J. Fluid Mech. (1998), *vol.* 370, *pp.* 149–174. Printed in the United Kingdom

Mean flow refraction effects on sound radiated from localized sources in a jet

By CHRISTOPHER K. W. TAM
AND LAURENT AURIAULT

Department of Mathematics, Florida State University, Tallahassee, FL 32306-4510, USA

(Received 22 November 1996 and in revised form 30 March 1998)

It is well-known that sound generated by localized sources embedded in a jet undergoes refraction as the acoustic waves propagate through the jet mean flow. For isothermal or hot jets, the effect of refraction causes the deflection of the radiated sound waves away from the jet flow direction. This gives rise to a cone of silence around the jet axis where there is a significant reduction in the radiated sound intensity. In this work, the mean flow refraction problem is investigated through the use of the reciprocity principle. Instead of the direct source Green's function, the adjoint Green's function with the source and observation points interchanged is used to quantify the effect of mean flow on sound radiation. One advantage of the adjoint Green's function is that the Green's functions for all the source locations in the jet radiating to a given direction in the far field can be obtained in a single calculation. This provides great savings in computational effort. Another advantage of the adjoint Green's function is that there is no singularity in the jet flow so that the problem can be solved numerically with axial as well as radial mean flow gradients included in a fairly straightforward manner. Extensive numerical computations have been carried out for realistic jet flow profiles with and without exercising the locally parallel flow approximation. It is concluded that the locally parallel flow approximation is valid as long as the direction of radiation is outside the cone of silence.

1. Introduction

It is well-known that the directivity of sound generated by a localized source inside a jet is significantly modified by the presence of the mean flow. Figure 1 illustrates the refraction of a ray of sound emitted by a point source S located in the mixing layer of a jet. To see why the ray is bent, one needs only to consider the propagation of the wave front AB. The point A moves at a speed equal to the local sound speed plus the local flow velocity of the jet. So does the point B. If the jet is nearly isothermal, then the speed of sound is the same at A and B. But the flow velocity at B is higher. As a result, as the wave front propagates it becomes tilted as $A'B'$. Obviously, this effect of refraction is even more pronounced for hot jets. In this case, the sound speed at B is higher than that at A. One of the important consequences of mean flow refraction is that less sound can be radiated in the direction of the jet flow. This creates a relatively quiet region around the jet axis commonly known as the 'cone of silence'. Experimentally, the presence of a cone of silence has been demonstrated by Atvars, Schubert & Ribner (1965). On the other hand, if the jet is very cold, the same argument would lead to the conclusion that sound rays would be bent toward the jet axis. This, in turn, leads to a large increase in sound intensity there. Grande (1965)

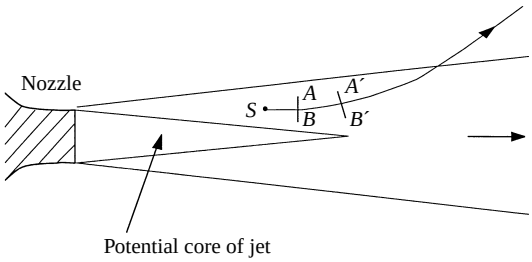

FIGURE 1. Schematic diagram showing the refraction of a ray of sound emitted by a localized source at S in a jet.

carried out such an experiment using a monopole source in a cold nitrogen jet. His measurements confirmed a very significant increase in the radiated sound intensity around the axial direction of the jet.

In the literature, there have been numerous investigations on the effects of mean flow refraction on the radiation of sound from localized noise sources in jets. Because of entrainment, the mean flow of a jet diverges in the axial direction. Thus, there are axial as well as radial gradients to be considered, although the former is much smaller than the latter. Because of this complexity in the mean flow profile, so far only approximate solutions are available. To render the problem tractable analytically, Mani (1976*a*, *b*) replaced the jet by a plug flow. In his model, the jet flow was assumed to be parallel and bounded by a vortex sheet. Goldstein (1975, 1976) considered parallel flow axisymmetric jets. He developed Green's functions for multipole sources valid at low frequency. Balsa (1976) and Goldstein (1982), on the other hand, investigated the high-frequency Green's function for parallel but not necessarily axisymmetric jets. Tester & Morfey (1976) and Balsa (1977) used a parallel flow model to construct approximate point source solutions of the flow equations in both the low- and high-frequency limits. At very high frequency, the acoustic wavelength is short. This allows the treatment of sound propagation by the method of geometric acoustics. Initial work was done by Schubert (1972). A much more general theory was later formulated by Durbin (1983*a*, *b*). Recently, Khavaran & Kresja (1993, 1994) and Khavaran (1996) applied this method to non-parallel non-axisymmetric jets. The approximate solutions mentioned above are generally useful within the intended range of validity. However, it is important to point out that almost all the approximate solutions fail near and inside the cone of silence. This is not surprising, for it is in the direction of the cone of silence that the effect of refraction is the largest and that both the axial and radial gradients of the mean flow must be taken into account.

Inside a jet, fine-scale turbulence is distributed over nearly its entire volume. Each local volume of fine-scale turbulence acts as an independent noise source. Thus, to find the noise radiated to a given direction in the far field, it is necessary to sum the contribution from each local volume of the jet as illustrated in figure 2. This requires the determination of the flow effects for each of these individual volume sources. This is an extremely laborious and time consuming process.

The primary objective of this investigation is to develop an efficient and accurate method for the computation of the flow refraction effect in jets with realistic mean flow profiles. To accomplish this, we will first introduce the idea of reciprocity and recast the refraction problem into a scattering/radiation (the adjoint) problem. The scattering/radiation problem is then solved by a computational aeroacoustics method.

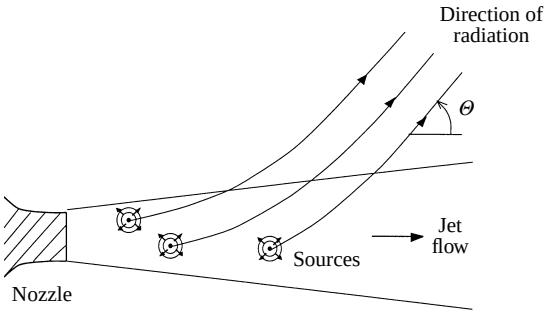

FIGURE 2. Distributed noise sources contributing to the radiation in a given direction.

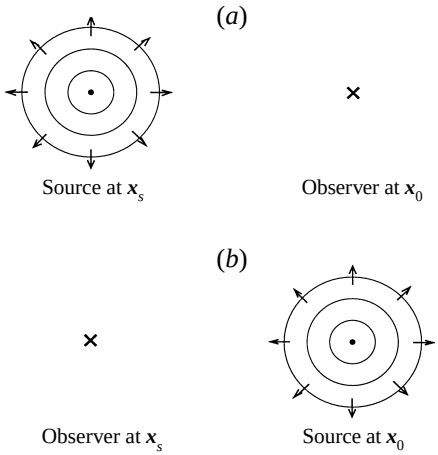

FIGURE 3. Monopole acoustic source radiation. (*a*) Source at $\boldsymbol{x}_s$, observer at $\boldsymbol{x}_0$. (*b*) Source at $\boldsymbol{x}_0$, observer at $\boldsymbol{x}_s$.

In many branches of mechanics, the reciprocity principle applies. However, the existence of a reciprocity principle has not been fully exploited in fluid mechanics and acoustics. Notable exceptions are the works of Cho (1980), Howe (1975, 1978, 1981) and Dowling (1983) in acoustics; Roberts (1960), Eckhaus (1965) and Chandrasekhar (1989) in hydrodynamic stability; and Hill (1995) in receptivity problems. To fix ideas, consider a time-periodic point source of sound located at $\boldsymbol{x}_s$ as shown in figure 3(*a*). Let $G(\boldsymbol{x}_0, \boldsymbol{x}_s, \omega)$ be the pressure associated with the sound field measured by an observer at $\boldsymbol{x}_0$. Mathematically, $G(\boldsymbol{x}_0, \boldsymbol{x}_s, \omega)$ is the Green's function of the wave equation and ω is the angular frequency of oscillation. (Note: we will use the notation that the first argument of the Green's function is the location of the observer and the second argument is the location of the source.) Now let us interchange the location of the sound source and the observer as shown in figure 3(*b*). Clearly, by symmetry the pressure measured by the observer, now at $\boldsymbol{x}_s$ while the source is at $\boldsymbol{x}_0$, is the same as before. That is,

$$G(\boldsymbol{x}_0, \boldsymbol{x}_s, \omega) = G(\boldsymbol{x}_s, \boldsymbol{x}_0, \omega). \tag{1}$$

Equation (1) is simply the statement that the Green's function $G(\boldsymbol{x}_0, \boldsymbol{x}_s, \omega)$ is self-adjoint or symmetric.

In the case of a sound source located inside a jet flow and an observer in the far field as illustrated in figure 4(*a*), the problem is not self-adjoint. This is because of the

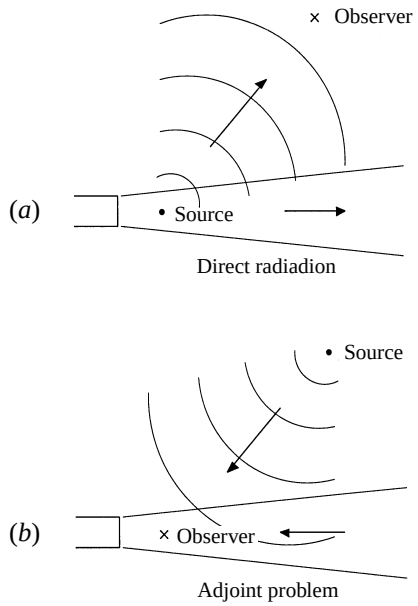

FIGURE 4. (*a*) The direct sound radiation problem. (*b*) The adjoint problem – a sound scattering problem.

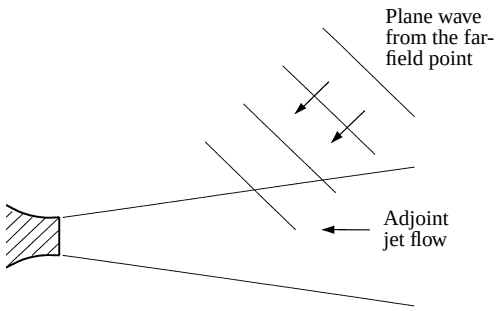

FIGURE 5. Sound scattering problem involving incident plane acoustic waves and adjoint jet flow.

presence of the jet mean flow. However, as we shall show in § 2 and § 3, it is possible to develop an adjoint problem with an adjoint mean flow such that the Green's functions with the locations of the source and observer interchanged are equal. That is, if $G_a(\boldsymbol{x}, \boldsymbol{x}_s, \omega)$ is the adjoint Green's function of figure 4(*b*), then

$$G(\boldsymbol{x}_0, \boldsymbol{x}_s, \omega) = G_a(\boldsymbol{x}_s, \boldsymbol{x}_0, \omega). \tag{2}$$

Clearly the adjoint problem is a sound scattering problem by the adjoint jet flow. For an observer at $\boldsymbol{x}_0$, located in the far field of the original problem, the sound waves emitted by the source in the adjoint problem are plane waves by the time they reach the vicinity of the jet. This is illustrated in figure 5. Now if the adjoint sound scattering problem is solved, then $G_a(\boldsymbol{x}_s, \boldsymbol{x}_0, \omega)$ is known for all $\boldsymbol{x}_s$ located in the jet. (Note: the point source is located at $\boldsymbol{x}_0$ for the adjoint problem.) But by (2) this is equal to $G(\boldsymbol{x}_0, \boldsymbol{x}_s, \omega)$. Thus, the direct radiation problem (radiate in the direction $\boldsymbol{x}_0$) from all possible noise source locations $\boldsymbol{x}_s$ inside the jet is found in

one single calculation. In this way, the laborious process of solving for $G(\boldsymbol{x}_0, \boldsymbol{x}_s, \omega)$ repeatedly by changing $\boldsymbol{x}_s$ over the entire volume of the jet is completely circumvented. For a specific example involving multiple point sources in a jet illustrating the enormous savings in computation by using the adjoint Green's function, see Appendix C.

The rest of this paper is as follows. In § 2, the adjoint Green's function problem for locally parallel flow jets is formulated and solved. In § 3, the case of non-parallel flow jets is considered. The adjoint problem is recast into a form suitable for a time marching numerical solution. Details about the numerical method are provided in § 4. Validation of the numerical solution and a parametric study of non-parallel flow effects are given in § 5. Finally, possible extension of the present method is discussed in § 6 of this paper.

2. Adjoint Green's function for locally parallel jet flows

In this section, we will formulate and solve the adjoint Green's function problem for locally parallel flow jets. The more general case of realistic divergent jets will be considered in the next section.

2.1. *Formulation of the adjoint problem*

Consider a parallel flow jet with the mean flow in the x-direction. We will denote the mean flow variables by an overbar. The mean flow velocity, pressure and density are $\overline{\boldsymbol{v}} = (\overline{u}(y,z), 0, 0)$, $\overline{p} = p_\infty$ (constant), $\overline{\rho} = \overline{\rho}(y,z)$. On starting with the linearized Euler equations, it is straightforward to find, by eliminating all other variables in favour of perturbation pressure p, a single third-order partial differential equation for p. Thus, by incorporating a point source term at $\boldsymbol{x}_s$ with time dependence of $\mathrm{e}^{-\mathrm{i}\omega t}$ on the right-hand side of the equation (i.e. $(1/2\pi)\delta(\boldsymbol{x}-\boldsymbol{x}_s)\,\mathrm{e}^{-\mathrm{i}\omega t}$; the factor $1/2\pi$ is added so that upon integrating over ω the time part becomes $\delta(t)$), the equation for the pressure Green's function is found. The equation for the spatial part of the Green's function, $G(\boldsymbol{x}, \boldsymbol{x}_s, \omega)$, is obtained by factoring out $\mathrm{e}^{-\mathrm{i}\omega t}$. It is

$$\left[\left(-\mathrm{i}\omega + \overline{u}\frac{\partial}{\partial x}\right)^3 + \frac{2\gamma\overline{p}}{\overline{\rho}}\left(\frac{\partial\overline{u}}{\partial y}\frac{\partial^2}{\partial x\partial y} + \frac{\partial\overline{u}}{\partial z}\frac{\partial^2}{\partial x\partial z}\right) - \frac{\gamma\overline{p}}{\overline{\rho}}\left(-\mathrm{i}\omega + \overline{u}\frac{\partial}{\partial x}\right)\nabla^2 + \frac{\gamma\overline{p}}{\overline{\rho}^2}\left(-\mathrm{i}\omega + \overline{u}\frac{\partial}{\partial x}\right)\left(\frac{\partial\overline{\rho}}{\partial y}\frac{\partial}{\partial y} + \frac{\partial\overline{\rho}}{\partial z}\frac{\partial}{\partial z}\right)\right] G(\boldsymbol{x}, \boldsymbol{x}_s, \omega) = \frac{1}{2\pi}\delta(\boldsymbol{x}-\boldsymbol{x}_s), \quad (3)$$

where γ is the ratio of the specific heats of the gas.

Now if we multiply (3) by $G_a(\boldsymbol{x}, \boldsymbol{x}_0, \omega)$ and integrate over all space, we obtain, after integration by parts and the use of the Green's theorem,

$$\iiint G(\boldsymbol{x}, \boldsymbol{x}_s, \omega)\left\{-\left(\mathrm{i}\omega + \overline{u}\frac{\partial}{\partial x}\right)^3 + 2\frac{\partial}{\partial y}\left(\frac{\gamma\overline{p}}{\overline{\rho}}\frac{\partial\overline{u}}{\partial y}\frac{\partial}{\partial x}\right) + 2\frac{\partial}{\partial z}\left(\frac{\gamma\overline{p}}{\overline{\rho}}\frac{\partial\overline{u}}{\partial z}\frac{\partial}{\partial x}\right) + \nabla^2\left[\frac{\gamma\overline{p}}{\overline{\rho}}\left(\mathrm{i}\omega + \overline{u}\frac{\partial}{\partial x}\right)\right] + \frac{\partial}{\partial y}\left[\frac{\gamma\overline{p}}{\overline{\rho}^2}\frac{\partial\overline{\rho}}{\partial y}\left(\mathrm{i}\omega + \overline{u}\frac{\partial}{\partial x}\right)\right] + \frac{\partial}{\partial z}\left[\frac{\gamma\overline{p}}{\overline{\rho}^2}\frac{\partial\overline{\rho}}{\partial z}\left(\mathrm{i}\omega + \overline{u}\frac{\partial}{\partial x}\right)\right]\right\} G_a(\boldsymbol{x}, \boldsymbol{x}_0, \omega)\,\mathrm{d}x\,\mathrm{d}y\,\mathrm{d}z = \frac{1}{2\pi}G_a(\boldsymbol{x}_s, \boldsymbol{x}_0, \omega). \quad (4)$$

At this time, we will specify $G_a(\boldsymbol{x}, \boldsymbol{x}_0, \omega)$ to be the adjoint Green's function satisfying the adjoint equation,

$$\left\{ -\left(\mathrm{i}\omega + \overline{u}\frac{\partial}{\partial x}\right)^3 + 2\frac{\partial}{\partial y}\left(\frac{\gamma\overline{p}}{\overline{\rho}}\frac{\partial\overline{u}}{\partial y}\frac{\partial}{\partial x}\right) + 2\frac{\partial}{\partial z}\left(\frac{\gamma\overline{p}}{\overline{\rho}}\frac{\partial\overline{u}}{\partial z}\frac{\partial}{\partial x}\right) + \nabla^2\left[\frac{\gamma\overline{p}}{\overline{\rho}}\left(\mathrm{i}\omega + \overline{u}\frac{\partial}{\partial x}\right)\right] + \frac{\partial}{\partial y}\left[\frac{\gamma\overline{p}}{\overline{\rho}^2}\frac{\partial\overline{\rho}}{\partial y}\left(\mathrm{i}\omega + \overline{u}\frac{\partial}{\partial x}\right)\right] + \frac{\partial}{\partial z}\left[\frac{\gamma\overline{p}}{\overline{\rho}^2}\frac{\partial\overline{\rho}}{\partial z}\left(\mathrm{i}\omega + \overline{u}\frac{\partial}{\partial x}\right)\right] \right\} G_a(\boldsymbol{x}, \boldsymbol{x}_0, \omega) = \frac{1}{2\pi}\delta(\boldsymbol{x} - \boldsymbol{x}_0). \tag{5}$$

Substituting (5) into (4), we find the reciprocity relation

$$G(\boldsymbol{x}_0, \boldsymbol{x}_s, \omega) = G_a(\boldsymbol{x}_s, \boldsymbol{x}_0, \omega). \tag{6}$$

It is straightforward to see from (5) that the jet flow direction of the adjoint problem is opposite to that of the direct radiation problem.

It will be assumed that $\boldsymbol{x}_0$, the direction of radiation for the direct problem and the source point for the adjoint problem, is in the far field away from the jet. Outside the jet, we have $\overline{u} = 0$, $\overline{p} = p_\infty$ and $\overline{\rho} = \rho_\infty$. Thus (5) simplifies to

$$\nabla^2 G_a(\boldsymbol{x}, \boldsymbol{x}_0, \omega) + \frac{\omega^2}{a_\infty^2} G_a(\boldsymbol{x}, \boldsymbol{x}_0, \omega) = \frac{1}{2\pi\mathrm{i}\omega a_\infty^2}\delta(\boldsymbol{x} - \boldsymbol{x}_0), \tag{7}$$

where $a_\infty = (\gamma p_\infty/\rho_\infty)^{1/2}$ is the ambient sound speed. The solution of (7), which satisfies the outgoing wave condition, is

$$G_a(\boldsymbol{x}, \boldsymbol{x}_0, \omega) = \frac{\mathrm{i}}{8\pi^2\omega a_\infty^2}\frac{\mathrm{e}^{\mathrm{i}\omega|\mathbf{x}-\mathbf{x}_0|/a}}{|\boldsymbol{x} - \boldsymbol{x}_0|} \tag{8}$$

where $|\boldsymbol{x} - \boldsymbol{x}_0|$ is the distance between $\boldsymbol{x}$ and $\boldsymbol{x}_0$.

For convenience, we will use a spherical coordinate system centred at the jet axis with the polar axis coinciding with the x-direction; R is the radial coordinate, Θ denotes the polar angle and ϕ the azimuthal angle measured from the (x, y)-plane. Without loss of generality, let $(R, \Theta, \phi = 0)$ be the spherical coordinates of $\boldsymbol{x}_0$. For very large R, the acoustic waves of the adjoint problem, when reaching the vicinity of the jet, are in the form of plane waves. Therefore, in the limit $R \to \infty$, (8) becomes

$$G_a(\boldsymbol{x}, \boldsymbol{x}_0, \omega) = \frac{\mathrm{i}}{8\pi^2\omega a_\infty^2}\frac{\exp\left(-\mathrm{i}\dfrac{\omega}{a_\infty}(x\cos\Theta + y\sin\Theta) + \mathrm{i}\dfrac{\omega}{a_\infty}R\right)}{R} \tag{9}$$

in the vicinity of the jet.

Now the adjoint Green's function problem can be recast into a wave scattering problem with (9) as the incident wave. The sum of the scattered waves and the incident wave satisfies the homogeneous form of equation (5). One advantage of solving the wave scattering problem instead of the original problem is that there is no source singularity (the delta function at the source) to deal with. This is especially helpful when a computational aeroacoustics method is used.

2.2. *Axisymmetric jets*

For axisymmetric jets, it would be natural to use a cylindrical coordinate system (r, ϕ, x) with the jet axis as the x-axis; y is related to r and ϕ by $y = r\cos\phi$. By replacing y in (9) with $r\cos\phi$, the incident plane wave in cylindrical coordinates is obtained. This plane wave may be expanded as a sum of cylindrical waves (see Magnus & Oberhettinger 1949). Hence

$$\underset{R\to\infty}{G_a}(\boldsymbol{x}, \boldsymbol{x}_0, \omega) = \frac{\exp\left(-\mathrm{i}\dfrac{\omega}{a_\infty}(x\cos\Theta - R)\right)}{8\pi^2\omega a_\infty^2 R}\sum_{m=0}^{\infty}(-\mathrm{i})^m\,\varepsilon_m J_m\left(\frac{\omega\sin\Theta}{a_\infty}r\right)\cos m\phi \quad (10)$$

where $\varepsilon_0 = 1$, $\varepsilon_m = 2$ for $m \geqslant 1$. $J_m(\ \ )$ is the mth-order Bessel function.

Outside the jet, i.e. at $r \geqslant R_0$ where $\bar{u} = 0$, $\bar{\rho} = \rho_\infty$, the scattered wave part of the adjoint Green's function, $G_a^{(s)}(\boldsymbol{x}, \boldsymbol{x}_0, \omega)$, can be found by separation of variables. Let

$$G_a^{(s)}(\boldsymbol{x}, \boldsymbol{x}_0, \omega) = \frac{\exp\left(-\mathrm{i}\dfrac{\omega}{a_\infty}(x\cos\Theta - R)\right)}{8\pi^2\omega a_\infty^2 R}\sum_{m=0}^{\infty}h_m(r)\cos m\phi. \quad (11)$$

The adjoint Green's function in this region ($r \geqslant R_0$) is related to $G_a^{(s)}(\boldsymbol{x}, \boldsymbol{x}_0, \omega)$ by

$$G_a(\boldsymbol{x}, \boldsymbol{x}_0, \omega) = \underset{R\to\infty}{G_a}(\boldsymbol{x}, \boldsymbol{x}_0, \omega) + G_a^{(s)}(\boldsymbol{x}, \boldsymbol{x}_0, \omega). \quad (12)$$

On substituting (12) into (7), it is straightforward to find that the equation for $h_m(r)$ is

$$\frac{\mathrm{d}^2 h_m}{\mathrm{d}r^2} + \frac{1}{r}\frac{\mathrm{d}h_m}{\mathrm{d}r} + \left(\frac{\omega^2\sin^2\Theta}{a_\infty^2} - \frac{m^2}{r^2}\right)h_m = 0. \quad (13)$$

The solution of (13) that satisfies the radiation boundary condition is $H_m^{(1)}\left((\omega\sin\Theta/a_\infty)r\right)$ where $H_m^{(1)}(\ \ )$ is the mth-order Hankel function of the first kind. Thus, outside the jet ($r \geqslant R_0$) the adjoint Green's function may be written in the form,

$$\underset{r\geqslant R_0}{G_a}(\boldsymbol{x}, \boldsymbol{x}_0, \omega) = \frac{\exp\left(-\mathrm{i}\dfrac{\omega}{a_\infty}(x\cos\Theta - R)\right)}{8\pi^2\omega a_\infty^2 R}\sum_{m=0}^{\infty}\left[(-\mathrm{i})^m\,\varepsilon_m J_m\left(\frac{\omega\sin\Theta}{a_\infty}r\right) + A_m H_m^{(1)}\left(\frac{\omega\sin\Theta}{a_\infty}r\right)\right]\cos m\phi, \quad (14)$$

where A_m ($m = 0, 1, 2, \ldots$) are arbitrary constants.

For $r \leqslant R_0$, the adjoint Green's function may be expanded in a Fourier Cosine series in ϕ:

$$\underset{r\leqslant R_0}{G_a}(\boldsymbol{x}, \boldsymbol{x}_0, \omega) = \frac{\exp\left(-\mathrm{i}\dfrac{\omega}{a_\infty}(x\cos\Theta - R)\right)}{8\pi^2\omega a_\infty^2 R}\sum_{m=0}^{\infty}f_m(r)\cos m\phi. \quad (15)$$

By substituting (15) into (5), rewritten in cylindrical coordinates, it is easy to find that

the equation for $f_m(r)$ is

$$\frac{\mathrm{d}^2 f_m}{\mathrm{d}r^2} + \left[\frac{-4\dfrac{\cos\Theta}{a_\infty}\dfrac{\mathrm{d}\,\overline{u}}{\mathrm{d}r}}{\left(1-\dfrac{\overline{u}\cos\Theta}{a_\infty}\right)} - \frac{1}{\overline{\rho}}\frac{\mathrm{d}\,\overline{\rho}}{\mathrm{d}r} + \frac{1}{r}\right]\frac{\mathrm{d}f_m}{\mathrm{d}r} + \left[\frac{\omega^2\left(1-\dfrac{\overline{u}\cos\Theta}{a_\infty}\right)^2}{\left(\dfrac{\gamma\,\overline{p}}{\overline{\rho}}\right)}\right.$$
$$\left. + \frac{3\left(\dfrac{1}{\overline{\rho}}\dfrac{\mathrm{d}\,\overline{\rho}}{\mathrm{d}r}\dfrac{\mathrm{d}\,\overline{u}}{\mathrm{d}r} - \dfrac{1}{r}\dfrac{\mathrm{d}\,\overline{u}}{\mathrm{d}r} - \dfrac{\mathrm{d}^2\overline{u}}{\mathrm{d}r^2}\right)\dfrac{\cos\Theta}{a_\infty}}{\left(1-\dfrac{\overline{u}\cos\Theta}{a_\infty}\right)} - \frac{m^2}{r^2} - \frac{\omega^2\cos^2\Theta}{a_\infty^2}\right] f_m = 0. \quad (16)$$

Unless a very special mean flow profile, $\overline{u}(r)$ and $\overline{\rho}(r)$, is chosen, (16) can only be integrated by numerical methods. This equation has a regular singular point at $r = 0$. For small r, a series solution of (16) that is bounded as $r \to 0$ is

$$f_m = a_m r^m + O\left(r^{m+2}\right). \quad (17)$$

To find $f_m(r)$, one can integrate (16) numerically using (17) as a starting solution. The numerical integration is to be continued until $r = R_0$ is reached, whereby the two unknown constants, A_m of (14) and a_m of (17), are adjusted so that the radial function and its derivative are equal to those of (14). This ensures that $G_a(\boldsymbol{x}, \boldsymbol{x}_0, \omega)$ and its derivatives are continuous. In this way, the adjoint Green's function is found. The accuracy of the solution is limited only by the accuracy of the numerical method used to integrate equation (16).

For axisymmetric jets, it turns out, the Green's function $G(\boldsymbol{x}, \boldsymbol{x}_s, \omega)$ governed by equation (3) can also be found by separation of variables after Fourier transform in x is first performed. We will let $\boldsymbol{x}_s = (r_s, \phi_s, x_s)$ in cylindrical coordinates and $\boldsymbol{x} = (R, \Theta, \phi)$ in spherical polar coordinates. In the limit $R \to \infty$, it is easy to show that the Green's function $G(\boldsymbol{x}, \boldsymbol{x}_s, \omega)$ (after the inverse Fourier transform integral has been evaluated by the method of stationary phase) has the form,

$$\underset{R\to\infty}{G}(r_s, \phi-\phi_s, x_s, R, \Theta, \omega) = \sum_{m=0}^{\infty}\frac{2}{R}c_m \exp\left(\mathrm{i}\frac{\omega}{a_\infty}R - \mathrm{i}\tfrac{1}{2}\pi(m+1)\right)\cos\left[m(\phi-\phi_s)\right], \quad (18)$$

where

$$c_m = \frac{-\mathrm{i}\exp\left(-\mathrm{i}\dfrac{\omega}{a_\infty}x_s\cos\Theta\right)\varepsilon_m g_m^{(i)}(r_s)}{(2\pi)^3\dfrac{\gamma\,\overline{p}(r_s)}{\overline{\rho}(r_s)}\left(1-\dfrac{\overline{u}(r_s)\cos\Theta}{a_\infty}\right)\omega r_s\left[\dfrac{\mathrm{d}g_m^{(0)}(r)}{\mathrm{d}r}g_m^{(i)}(r) - \dfrac{\mathrm{d}g_m^{(i)}(r)}{\mathrm{d}r}g_m^{(0)}(r)\right]_{r=r_s}}.$$

The functions $g_m^{(i)}(r)$ and $g_m^{(0)}(r)$ are solutions of the equation

$$\frac{\mathrm{d}^2 g_m}{\mathrm{d}r^2} + \left[\frac{1}{r} + \frac{2\cos\Theta\dfrac{\mathrm{d}\,\overline{u}}{\mathrm{d}r}}{a_\infty\left(1-\dfrac{\overline{u}\cos\Theta}{a_\infty}\right)} - \frac{1}{\overline{\rho}}\frac{\mathrm{d}\,\overline{\rho}}{\mathrm{d}r}\right]\frac{\mathrm{d}g_m}{\mathrm{d}r}$$
$$+ \left[\frac{\omega^2\left(1-\dfrac{\overline{u}\cos\Theta}{a_\infty}\right)^2}{\left(\gamma\,\overline{p}/\overline{\rho}\right)} - \frac{m^2}{r^2} - \frac{\omega^2\cos^2\Theta}{a_\infty^2}\right] g_m = 0 \quad (19)$$

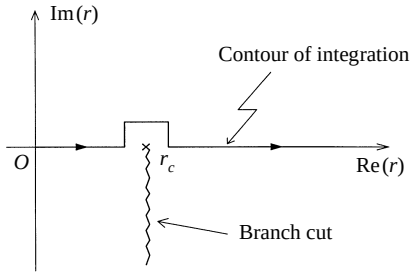

FIGURE 6. Contour of integation in the complex r-plane deformed above the critical point $r = r_c$ for velocity profiles with $\bar{u}' < 0$.

in the range $r \leqslant r_s$ and $r \geqslant r_s$ respectively satisfying the conditions

$$g_m^{(i)}(r) \underset{r\to 0}{\to} O(r^m), \quad g_m^{(0)}(r) \underset{r\to\infty}{\to} H_m^{(1)}\left(\frac{\omega \sin\Theta}{a_\infty} r\right).$$

It is to be noted that for high-speed jets both equations (16) for the adjoint Green's function and (19) for the direct Green's function have a regular singular point at $r = r_c$ where $\bar{u}(r_c)(\cos\Theta/a_\infty) = 1$. The correct treatment of this singularity is to reformulate the problem as an initial value problem or to regard ω as the Laplace transform with a small positive imaginary part as discussed by Tam (1975) and Tam & Morris (1980). For a typical jet velocity profile with $\bar{u}' < 0$, equations (16) and (19) are to be integrated over the deformed contour above the critical point (and the branch cut) as shown in figure 6.

Extensive numerical computations of the adjoint Green's function $G_a(\boldsymbol{x}_s, \boldsymbol{x}_0, \omega)$ of (15) and the direct Green's function $G(\boldsymbol{x}_0, \boldsymbol{x}_s, \omega)$ of (18) with $\boldsymbol{x}_0$ in the far acoustic field for a number of realistic mean jet velocity and density profiles over a wide range of Strouhal number $\mathrm{St} = fu_j/D$ (where f, u_j and D are the frequency, the fully expanded jet velocity and diameter respectively) have been carried out. It has been found, owing to the argument of the Bessel functions being large, that only the first 4 to 5 azimuthal modes are needed to provide an accuracy of 3 to 4 significant figures. To the accuracy of the numerical integration used, the reciprocity relation (6) has been found to be true for all the cases. This is so even for directions of radiation inside the cone of silence. In carrying out the numerical computation the advantage of using the adjoint Green's function becomes very apparent. It takes only one integration of (16) to provide the flow refraction information for all the sources located at various radial distance from the jet axis. There is a great saving in computation effort.

3. The adjoint problem for non-parallel jet flows

3.1. *The adjoint problem*

For non-parallel jet flows, it is not possible, because of the presence of axial gradient terms, to reduce the linearized Euler equations to a single equation. Under this circumstance, it is found that it would be best to work with the first-order system of equations. In this work, we are interested in the mean flow refraction effect on the noise from fine-scale turbulence. Since fine-scale turbulence has no sources of mass, it is, therefore, sufficient to consider only the Green's functions associated with fluctuating momentum sources. In other words, the governing equations to be

solved are the linearized Euler and energy equations with a time-periodic source term, $(1/2\pi)\delta(\boldsymbol{x}-\boldsymbol{x}_s)\,\mathrm{e}^{-\mathrm{i}\omega t}$, added to the right-hand side of the momentum equations.

In Appendix A, the adjoint equations in the most general case including the presence of solid surfaces are derived. For axisymmetric jets, the linearized Euler equations with momentum source terms and their adjoint are somewhat simpler. For convenience, we will use superscript (n) with $n = 1, 2$ or 3 to denote the Green's function variables corresponding to a time-periodic source in the radial, azimuthal and axial momentum equations. A superscript (a) will be used to denote the adjoint variables. Upon factoring out the time factor $\mathrm{e}^{-\mathrm{i}\omega t}$ (i.e. only the spatial part is retained) these equations (equations for the Green's functions) in cylindrical coordinates are

$$-\mathrm{i}\omega\rho^{(n)} + \frac{1}{r}\frac{\partial}{\partial r}\left[\left(\overline{\rho}\,v^{(n)} + \rho^{(n)}\,\overline{v}\right)r\right] + \frac{1}{r}\frac{\partial}{\partial\phi}\left(\overline{\rho}\,w^{(n)}\right) + \frac{\partial}{\partial x}\left(\overline{\rho}\,u^{(n)} + \rho^{(n)}\,\overline{u}\right) = 0, \quad (20a)$$

$$-\mathrm{i}\omega\,\overline{\rho}\,v^{(n)} + \overline{\rho}\,\overline{v}\,\frac{\partial v^{(n)}}{\partial r} + \overline{\rho}\,v^{(n)}\frac{\partial\,\overline{v}}{\partial r} + \overline{\rho}\,\overline{u}\,\frac{\partial v^{(n)}}{\partial x} + \overline{\rho}\,u^{(n)}\frac{\partial\,\overline{v}}{\partial x} + \rho^{(n)}\left(\overline{v}\,\frac{\partial\,\overline{v}}{\partial r} + \overline{u}\,\frac{\partial\,\overline{v}}{\partial x}\right) + \frac{\partial p^{(n)}}{\partial r} = \frac{\delta_{n1}}{2\pi}\delta(\boldsymbol{x}-\boldsymbol{x}_s), \quad (20b)$$

$$-\mathrm{i}\omega\,\overline{\rho}\,w^{(n)} + \overline{\rho}\,\overline{v}\,\frac{\partial w^{(n)}}{\partial r} + \overline{\rho}\,\overline{u}\,\frac{\partial w^{(n)}}{\partial x} + \frac{\overline{\rho}\,\overline{v}\,w^{(n)}}{r} + \frac{1}{r}\frac{\partial p^{(n)}}{\partial\phi} = \frac{\delta_{n2}}{2\pi}\delta(\boldsymbol{x}-\boldsymbol{x}_s), \quad (20c)$$

$$-\mathrm{i}\omega\,\overline{\rho}\,u^{(n)} + \overline{\rho}\,\overline{v}\,\frac{\partial u^{(n)}}{\partial r} + \overline{\rho}\,v^{(n)}\frac{\partial\,\overline{u}}{\partial r} + \overline{\rho}\,\overline{u}\,\frac{\partial u^{(n)}}{\partial x} + \overline{\rho}\,u^{(n)}\frac{\partial\,\overline{u}}{\partial x}, + \rho^{(n)}\left(\overline{v}\,\frac{\partial\,\overline{u}}{\partial r} + \overline{u}\,\frac{\partial\,\overline{u}}{\partial x}\right) + \frac{\partial p^{(n)}}{\partial x} = \frac{\delta_{n3}}{2\pi}\delta(\boldsymbol{x}-\boldsymbol{x}_s) \quad (20d)$$

$$-\mathrm{i}\omega p^{(n)} + \overline{v}\,\frac{\partial p^{(n)}}{\partial r} + v^{(n)}\frac{\partial\,\overline{p}}{\partial r} + \overline{u}\,\frac{\partial p^{(n)}}{\partial x} + u^{(n)}\frac{\partial\,\overline{p}}{\partial x} + \gamma\,\overline{p}\left[\frac{1}{r}\frac{\partial\left(v^{(n)}r\right)}{\partial r} + \frac{1}{r}\frac{\partial w^{(n)}}{\partial\phi} + \frac{\partial u^{(n)}}{\partial x}\right] + \gamma p^{(n)}\left[\frac{1}{r}\frac{\partial\left(\overline{v}\,r\right)}{\partial r} + \frac{\partial\,\overline{u}}{\partial x}\right] = 0, \quad (20e)$$

where $u^{(n)}$, $v^{(n)}$ and $w^{(n)}$ are the velocity components in the x-, r- and ϕ-directions respectively; δ_{nm} is the Kronecker delta.

The adjoint equations can be derived as in Appendix A. They are

$$-\mathrm{i}\omega\rho^{(a)} - \overline{v}\,\frac{\partial\rho^{(a)}}{\partial r} - \overline{u}\,\frac{\partial\rho^{(a)}}{\partial x} + v^{(a)}\left(\overline{v}\,\frac{\partial\,\overline{v}}{\partial r} + \overline{u}\,\frac{\partial\,\overline{v}}{\partial x}\right) + u^{(a)}\left(\overline{v}\,\frac{\partial\,\overline{u}}{\partial r} + \overline{u}\,\frac{\partial\,\overline{u}}{\partial x}\right) = 0, \quad (21a)$$

$$-\mathrm{i}\omega\,\overline{\rho}\,v^{(a)} - \overline{\rho}\,\frac{\partial\rho^{(a)}}{\partial r} - \frac{1}{r}\frac{\partial}{\partial r}\left(\overline{\rho}\,\overline{v}\,v^{(a)}r\right) + \overline{\rho}\,v^{(a)}\frac{\partial\,\overline{v}}{\partial r} - \frac{\partial}{\partial x}\left(\overline{\rho}\,\overline{u}\,v^{(a)}\right) + \overline{\rho}\,u^{(a)}\frac{\partial\,\overline{u}}{\partial r} + (1-\gamma)\,p^{(a)}\frac{\partial\,\overline{p}}{\partial r} - \gamma\,\overline{p}\,\frac{\partial p^{(a)}}{\partial r} = 0, \quad (21b)$$

$$-\mathrm{i}\omega\,\overline{\rho}\,w^{(a)} - \frac{\overline{\rho}}{r}\frac{\partial\rho^{(a)}}{\partial\phi} - \frac{1}{r}\frac{\partial}{\partial r}\left(\overline{\rho}\,\overline{v}\,rw^{(a)}\right) - \frac{\partial}{\partial x}\left(\overline{\rho}\,\overline{u}\,w^{(a)}\right) + \frac{\overline{\rho}\,\overline{v}\,w^{(a)}}{r} - \frac{\gamma\,\overline{p}}{r}\frac{\partial p^{(a)}}{\partial\phi} = 0, \quad (21c)$$

$$-\mathrm{i}\omega\,\overline{\rho}\,u^{(a)}-\overline{\rho}\,\frac{\partial\rho^{(a)}}{\partial x}+\overline{\rho}\,v^{(a)}\frac{\partial\,\overline{v}}{\partial x}-\frac{1}{r}\frac{\partial}{\partial r}\left(\overline{\rho}\,\overline{v}\,ru^{(a)}\right)-\frac{\partial}{\partial x}\left(\overline{\rho}\,\overline{u}\,u^{(a)}\right)$$
$$+\overline{\rho}\,u^{(a)}\frac{\partial\,\overline{u}}{\partial x}+(1-\gamma)\,p^{(a)}\frac{\partial\,\overline{p}}{\partial x}-\gamma\,\overline{p}\,\frac{\partial p^{(a)}}{\partial x}=0, \tag{21d}$$

$$-\mathrm{i}\omega p^{(a)}-\frac{1}{r}\frac{\partial}{\partial r}\left(v^{(a)}r\right)-\frac{1}{r}\frac{\partial w^{(a)}}{\partial\phi}-\frac{\partial u^{(a)}}{\partial x}-\frac{1}{r}\frac{\partial}{\partial r}\left(\overline{v}\,p^{(a)}r\right)$$
$$-\frac{\partial}{\partial x}\left(\overline{u}\,p^{(a)}\right)+\gamma p^{(a)}\left(\frac{1}{r}\frac{\partial\,(\overline{v}\,r)}{\partial r}+\frac{\partial\,\overline{u}}{\partial x}\right)=\frac{1}{2\pi}\delta\,(\boldsymbol{x}-\boldsymbol{x}_0)\,. \tag{21e}$$

It is easy to establish (see Appendix A) that the reciprocity relation between the original Green's function variables and the adjoint variables are

$$p^{(1)}\,(\boldsymbol{x}_0,\boldsymbol{x}_s,\omega)=v^{(a)}\,(\boldsymbol{x}_s,\boldsymbol{x}_0,\omega)\,, \tag{22}$$
$$p^{(2)}\,(\boldsymbol{x}_0,\boldsymbol{x}_s,\omega)=w^{(a)}\,(\boldsymbol{x}_s,\boldsymbol{x}_0,\omega)\,, \tag{23}$$
$$p^{(3)}\,(\boldsymbol{x}_0,\boldsymbol{x}_s,\omega)=u^{(a)}\,(\boldsymbol{x}_s,\boldsymbol{x}_0,\omega)\,. \tag{24}$$

It is worthwhile to mention that in the case of locally parallel flow jets with $\overline{u}=\overline{u}\,(r)$, $\overline{v}=\overline{w}=0$, $\overline{\rho}=\overline{\rho}\,(r)$ and $\overline{p}=p_\infty$, the adjoint equations simplify to

$$-\mathrm{i}\omega\,\overline{\rho}\,u^{(a)}-\overline{\rho}\,\overline{u}\,\frac{\partial u^{(a)}}{\partial x}-\gamma p_\infty\frac{\partial p^{(a)}}{\partial x}=0, \tag{25a}$$

$$-\mathrm{i}\omega\,\overline{\rho}\,v^{(a)}-\overline{\rho}\,\overline{u}\,\frac{\partial v^{(a)}}{\partial x}+\overline{\rho}\,u^{(a)}\frac{\partial\,\overline{u}}{\partial r}-\gamma p_\infty\frac{\partial p^{(a)}}{\partial r}=0, \tag{25b}$$

$$-\mathrm{i}\omega\,\overline{\rho}\,w^{(a)}-\overline{\rho}\,\overline{u}\,\frac{\partial w^{(a)}}{\partial x}-\frac{\gamma p_\infty}{r}\frac{\partial p^{(a)}}{\partial\phi}=0, \tag{25c}$$

$$-\mathrm{i}\omega p^{(a)}-\overline{u}\,\frac{\partial p^{(a)}}{\partial x}-\left[\frac{1}{r}\frac{\partial}{\partial r}\left(rv^{(a)}\right)+\frac{1}{r}\frac{\partial w^{(a)}}{\partial\phi}+\frac{\partial u^{(a)}}{\partial x}\right]=\frac{1}{2\pi}\delta\,(\boldsymbol{x}-\boldsymbol{x}_0)\,. \tag{25d}$$

For $\boldsymbol{x}_0$ located outside the jet, it can easily be shown that (25) can be reduced to a single equation for $p^{(a)}$. The adjoint problem can then be solved by the method of separation of variables as discussed in § 2.2.

For the jet noise problem, interest is in the case where $\boldsymbol{x}_0\,(R,\,\Theta,\,\phi=0)$ is in the far field, i.e. $R\to\infty$. Outside the jet, we have $\overline{u}=\overline{v}=\overline{w}=0$, $\overline{\rho}=\overline{\rho}_\infty$, $\overline{p}=p_\infty$. Equation (21) reduces to

$$\rho^{(a)}=0,\quad \boldsymbol{v}^{(a)}=\frac{\mathrm{i}a_\infty^2}{\omega}\nabla p^{(a)}, \tag{26}$$

$$\nabla^2p^{(a)}+\frac{\omega^2}{a_\infty^2}p^{(a)}=\frac{\mathrm{i}\omega}{2\pi a_\infty^2}\delta\,(\boldsymbol{x}-\boldsymbol{x}_0)\,. \tag{27}$$

On following the steps from equation (7) to equation (10), the solution of (27) in cylindrical coordinates may be written in the form

$$\underset{R\to\infty}{p^{(a)}}\,(\boldsymbol{x},\boldsymbol{x}_0,\omega)=\frac{-\mathrm{i}\omega}{8\pi^2a_\infty^2R}\exp\left(\mathrm{i}\frac{\omega}{a_\infty}\,(R-x\cos\Theta)\right)\sum_{m=0}^{\infty}(-\mathrm{i})^m\,\varepsilon_mJ_m\left(\frac{\omega\sin\Theta}{a_\infty}r\right)\cos m\phi. \tag{28}$$

The corresponding adjoint velocity field given by (26) can also be written out explicitly by simple differentiation.

3.2. *Time-domain formulation*

An analytic solution of equation (21) for the adjoint Green's function is unlikely to be found. We propose to solve the set of equations by a numerical time marching scheme. To do so, we will first recast the governing equations into a time-domain problem. The time-domain adjoint variables, labelled with a tilde, are defined by

$$\left.\begin{aligned}\tilde{\boldsymbol{v}}^{(a)}(\boldsymbol{x},\boldsymbol{x}_0,t) &= \boldsymbol{v}^{(a)}(\boldsymbol{x},\boldsymbol{x}_0,\omega)\,\mathrm{e}^{-\mathrm{i}\omega t},\\ \tilde{p}^{(a)}(\boldsymbol{x},\boldsymbol{x}_0,t) &= p^{(a)}(\boldsymbol{x},\boldsymbol{x}_0,\omega)\,\mathrm{e}^{-\mathrm{i}\omega t},\\ \tilde{\rho}^{(a)}(\boldsymbol{x},\boldsymbol{x}_0,t) &= \rho^{(a)}(\boldsymbol{x},\boldsymbol{x}_0,\omega)\,\mathrm{e}^{-\mathrm{i}\omega t}.\end{aligned}\right\} \tag{29}$$

The equations for the time-domain variables are obtained by replacing $-\mathrm{i}\omega$ in equation (21) by $\partial/\partial t$ and adding $\mathrm{e}^{-\mathrm{i}\omega t}$ to the delta function on the right-hand side. Outside the jet, the non-homogeneous solution of these equations is given by (28) multiplied by $\mathrm{e}^{-\mathrm{i}\omega t}$ and the corresponding adjoint velocity components. We may consider this non-homogeneous solution as the incident acoustic wave generated by the source located at $\boldsymbol{x}_0$ $(R, \Theta, \phi = 0)$ with $R \to \infty$. The full solution then can be divided into two parts, namely the incident wave solution plus a radiation solution that satisfies the outgoing wave condition away from the jet. On expanding both parts of the solution as Fourier series in the azimuthal variable ϕ, the full solution may be written in the form

$$\begin{bmatrix}\tilde{p}^{(a)}\\ \tilde{u}^{(a)}\\ \tilde{v}^{(a)}\\ \tilde{w}^{(a)}\\ \tilde{\rho}^{(a)}\end{bmatrix}_{R\to\infty} = \frac{\mathrm{e}^{\mathrm{i}\omega R/a_\infty}}{8\pi^2 R}\sum_{m=0}^{\infty}(-\mathrm{i})^m\,\varepsilon_m\left\{\begin{bmatrix}-\dfrac{\mathrm{i}\omega}{a_\infty^2}J_m\left(\dfrac{\omega\sin\Theta}{a_\infty}r\right)\cos m\phi\\ -\dfrac{\mathrm{i}\omega\cos\Theta}{a_\infty}J_m\left(\dfrac{\omega\sin\Theta}{a_\infty}r\right)\cos m\phi\\ \dfrac{\omega\sin\Theta}{a_\infty}J_m'\left(\dfrac{\omega\sin\Theta}{a_\infty}r\right)\cos m\phi\\ -\dfrac{m}{r}J_m\left(\dfrac{\omega\sin\Theta}{a_\infty}r\right)\sin m\phi\\ 0\end{bmatrix}\right.$$

$$\left.\times\exp\left(-\mathrm{i}\omega\left(\frac{x\cos\Theta}{a_\infty}+t\right)\right)+\begin{bmatrix}\hat{p}_m(r,x,t)\cos m\phi\\ \hat{u}_m(r,x,t)\cos m\phi\\ \hat{v}_m(r,x,t)\cos m\phi\\ \hat{w}_m(r,x,t)\sin m\phi\\ \hat{\rho}_m(r,x,t)\cos m\phi\end{bmatrix}\right\}. \tag{30}$$

The first term on the right-hand side of (30) is the incident wave solution (the inhomogeneous solution (28) and the corresponding adjoint velocity components). The second term is the still unknown radiation solution.

By substituting (30) into the equations for the time-domain variables, we find that the equations for $(\hat{p}_m, \hat{u}_m, \hat{v}_m, \hat{w}_m, \hat{\rho}_m)$ are

$$\frac{\partial\hat{\rho}_m}{\partial t}-\bar{v}\frac{\partial\hat{\rho}_m}{\partial r}-\bar{u}\frac{\partial\hat{\rho}_m}{\partial x}+\left(\bar{v}\frac{\partial\bar{v}}{\partial r}+\bar{u}\frac{\partial\bar{v}}{\partial x}\right)\hat{v}_m+\left(\bar{v}\frac{\partial\bar{u}}{\partial r}+\bar{u}\frac{\partial\bar{u}}{\partial x}\right)\hat{u}_m = I_1, \tag{31a}$$

$$\bar{\rho}\frac{\partial\hat{u}_m}{\partial t}-\bar{\rho}\frac{\partial\hat{\rho}_m}{\partial x}+\bar{\rho}\frac{\partial\bar{v}}{\partial x}\hat{v}_m-\frac{1}{r}\frac{\partial}{\partial r}(\bar{\rho}\bar{v}r\hat{u}_m)-\bar{u}\frac{\partial}{\partial x}(\bar{\rho}\hat{u}_m)$$
$$-(\gamma-1)\frac{\partial\bar{p}}{\partial x}\hat{p}_m-\gamma\bar{p}\frac{\partial\hat{p}_m}{\partial x} = I_2, \tag{31b}$$

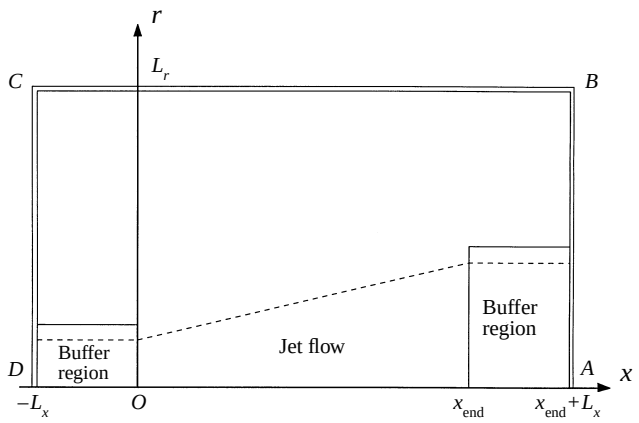

FIGURE 7. The computation domain in physical space.

$$\overline{\rho}\frac{\partial \widehat{v}_m}{\partial t} - \overline{\rho}\frac{\partial \widehat{\rho}_m}{\partial r} - \frac{\overline{v}\,\partial}{r\partial r}(\overline{\rho}\,\overline{v}_m r) - \frac{\partial}{\partial x}(\overline{\rho}\,\overline{u}\,\widehat{v}_m) + \overline{\rho}\frac{\partial \overline{u}}{\partial r}\widehat{u}_m - (\gamma-1)\frac{\partial \overline{p}}{\partial r}\widehat{p}_m - \gamma\,\overline{p}\frac{\partial \widehat{p}_m}{\partial r} = I_3, \tag{31c}$$

$$\overline{\rho}\frac{\partial \widehat{w}_m}{\partial t} + \frac{m}{r}\overline{\rho}\,\widehat{\rho}_m - \frac{\partial(\overline{\rho}\,\overline{v}\,\widehat{w}_m)}{\partial r} - \frac{\partial}{\partial x}(\overline{\rho}\,\overline{u}\,\widehat{w}_m) + \frac{\gamma\,\overline{p}\,m}{r}\widehat{p}_m = I_4, \tag{31d}$$

$$\frac{\partial \widehat{p}_m}{\partial t} - \frac{1}{r}\frac{\partial(\widehat{v}_m r)}{\partial r} - \frac{m}{r}\widehat{w}_m - \frac{\partial \widehat{u}_m}{\partial x} - \frac{1}{r}\frac{\partial(\overline{v}\,\widehat{p}_m r)}{\partial r} - \frac{\partial}{\partial x}(\overline{u}\,\widehat{p}_m) + \gamma\,\widehat{p}_m\left(\frac{\partial \overline{v}}{\partial r} + \frac{\overline{v}}{r} + \frac{\partial \overline{u}}{\partial x}\right) = I_5. \tag{31e}$$

The non-homogeneous terms I_1, I_2, I_3, I_4 and I_5 on the right-hand side of (31) are given in Appendix B. Equation (31) involves two space coordinates. A way to solve these equations numerically by time marching to a periodic solution is discussed in the next section.

4. Numerical implementation

The time-periodic solution of equation (31) that satisfies radiation boundary condition far away from the jet can be calculated numerically in a relatively straightforward manner by a number of methods. Therefore, only the pertinent details of the numerical computation are presented here.

One of the main reasons for reformulating the adjoint problem into a time marching radiation problem (instead of a scattering problem) is that the solution of such a problem inside the jet would not be greatly affected if part of the jet, away from the location where the solution is sought, is cut off smoothly. This can easily be understood by recalling that the effect of the mean flow on acoustic radiation is primarily refraction. As long as the mean flow gradient is smooth, there is very little backscattering. That is to say, there is an absence of back influence in the wave radiation process. This is important, for all numerical solutions must use a finite computation domain that requires the jet flow to be cut off in some way.

Figure 7 shows the computation domain in physical space. In our numerical

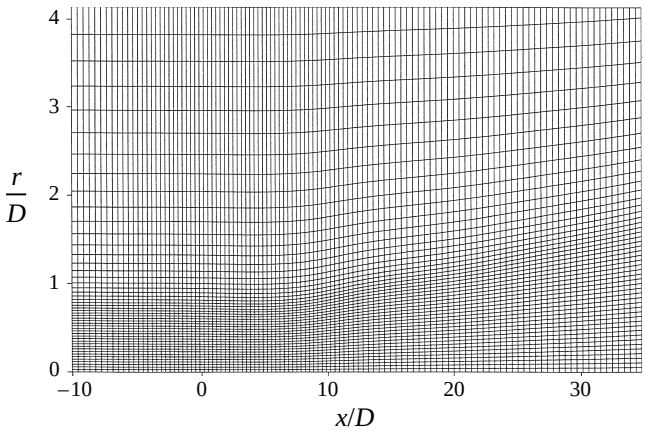

FIGURE 8. Grid lines (ξ, η) in the physical domain inside and in the near field of the jet flow (every second line is shown).

computation, the size of the computational domain excluding the two buffer regions is $25D$ by $15D$ ($x_{\text{end}} = 25D$, $L_r = 15D$) where D is the jet diameter. The mean flow of the jet is calculated by the parabolized marching scheme of Thies & Tam (1996). In the work of Thies & Tam, a modified $k - \varepsilon$ model is used to simulate the effect of turbulence. In the two buffer regions, the mean flow of the jet is artificially brought to zero very gradually. The size of these regions, L_x, used in this work is allowed to vary with frequency. In general, L_x is taken to be more than $10D$.

In high-speed jets, there is a strong shear gradient in the jet mixing layer. Near the nozzle exit the mixing layer is thin so that the shear gradient is especially large. To ensure that enough mesh points are located inside the mixing layer to provide adequate resolution, the physical domain is mapped into the computation domain by means of a radial and an axial mapping,

$$\eta = \eta(r), \quad \xi = \xi(x). \tag{32}$$

A typical map of constant η and ξ lines is shown in figure 8. The radial mapping is designed so that there are at least 20 mesh points in the jet mixing layer.

To solve equation (31) in the time domain, it is first rewritten in the (ξ, η)-coordinates. Then it is discretized according to the dispersion-relation-preserving (DRP) time marching scheme (see Tam & Webb 1993 and Tam 1995). A seven-point central difference stencil with optimized stencil coefficients is used to approximate spatial derivatives. A four-level optimized finite difference scheme is used for time marching. Because of the existence of strong shear gradients in the mixing layer of the jet, spurious numerical waves are expected to be generated as the sound waves pass through the region. To eliminate these spurious numerical waves, artificial damping terms (see Tam, Webb & Dong 1993 and Tam 1995) are added to each of the equations. The mesh Reynolds number, $R_{\Delta x} = a_\infty \Delta x / v_a$, where v_a is the artificial numerical viscosity, Δx is the mesh size in the physical space ($\Delta x = \Delta\xi / |\partial\xi / \partial x|$), is taken to be 10. In the interior of the computation domain, a seven-point damping stencil is used. Near the jet axis, the value of the inverse mesh Reynolds number is increased to 0.2. This value is transitioned to the general value of 0.1 by means of a Gaussian curve with a half-width of 3 mesh spacings.

Along the boundary $ABCD$ in figure 7, a set of radiation/outflow boundary

conditions for equation (31), derived in the same way as Tam & Webb (1993), are used. The purpose of the radiation boundary condition is to allow the sound waves to exit the computation domain with minimum reflection. Radiation/outflow boundary conditions, which are based on the asymptotic solutions of the governing equations, have been found by Hixson, Shih & Mankbadi (1995) to perform better than radiation boundary conditions based on the method of characteristics or Fourier expansion. Equation (31) is singular at the jet axis. Numerical methods cannot handle such singularity. In the present work, the singular terms are first replaced by their formal limits as $r \to 0$ before discretization. For instance, the term $\tilde{v}^{(a)}/r$ in (31*e*) becomes in the limit $r \to 0$

$$\lim_{r\to 0} \frac{\tilde{v}^{(a)}}{r} = \left.\frac{\partial \tilde{v}^{(a)}}{\partial r}\right|_{r=0}.$$

Thus a difference approximation of $\partial \tilde{v}^{(a)}/\partial r$ at $r = 0$ is used instead of $\tilde{v}^{(a)}/r$.

As mentioned above, one reason for incorporating the buffer regions in the computation domain, see figure 7, is to provide space to reduce the mean flow to zero gradually. It turns out that the buffer regions are also used for another important function. It is well-known that a jet is subjected to Kelvin–Helmholtz instability. This is a convective instability. That is, the unstable waves will propagate away from the region where they were generated. The time-domain adjoint equations (31) support the adjoint instability waves that have the same growth and propagation characteristics as the original Kelvin–Helmholtz instability. Computationally, it is important not to exite these instability waves for otherwise they would overwhelm the numerical solution. The forcing function of (31) is the incident acoustic wave. Its wavelength is much longer than the instability wave at the same frequency. Thus, the time-steady forcing would not excite the adjoint instability wave unless in regions of rapid changes in the mean flow. It is found that even though the mean flow is reduced to zero smoothly in the buffer regions, instability waves are, nevertheless, excited. To eliminate these waves immediately, constant damping terms are added to equation (31) in the buffer regions. The magnitude of these terms is adjusted so that the excited instability waves are damped out before propagating out of these regions.

In using the present time marching numerical method, the computation starts with zero initial conditions. The transient solution either propagates out of the computation domain or is being damped out in the buffer regions. In all the cases considered, the computation is continued until a time-periodic solution is attained.

The finite difference computer code that solves (31) has been validated by applying it to locally parallel flow jets and comparing the numerical results with the parallel flow jet solutions. For parallel flow jets, the adjoint is given by the solution of (25). This set of equations can be reduced to an ordinary differential equation by the method of separation of variables. The ordinary differential equation can be integrated numerically to high precision by using very small integration steps. We may regard this solution as nearly exact. Figure 9 shows a comparison of the real and imaginary part of $p^{(a)}(\boldsymbol{x}, \boldsymbol{x}_0, \omega)$ for a Mach 0.9 jet at a temperature ratio of 2.0 as calculated by the time marching code and the nearly exact parallel flow solution. The mean flow profile used corresponds to that at $x/D = 6$ of a divergent jet. The Strouhal number, $St = fD/u_j$, is 0.3. As can be seen there is excellent agreement between the numerically exact parallel flow solution and the time-domain finite difference solution. Extensive comparisons similar to figure 9 have been carried out over a range of jet Mach number, temperature ratio and axial location of the jet. Good agreements

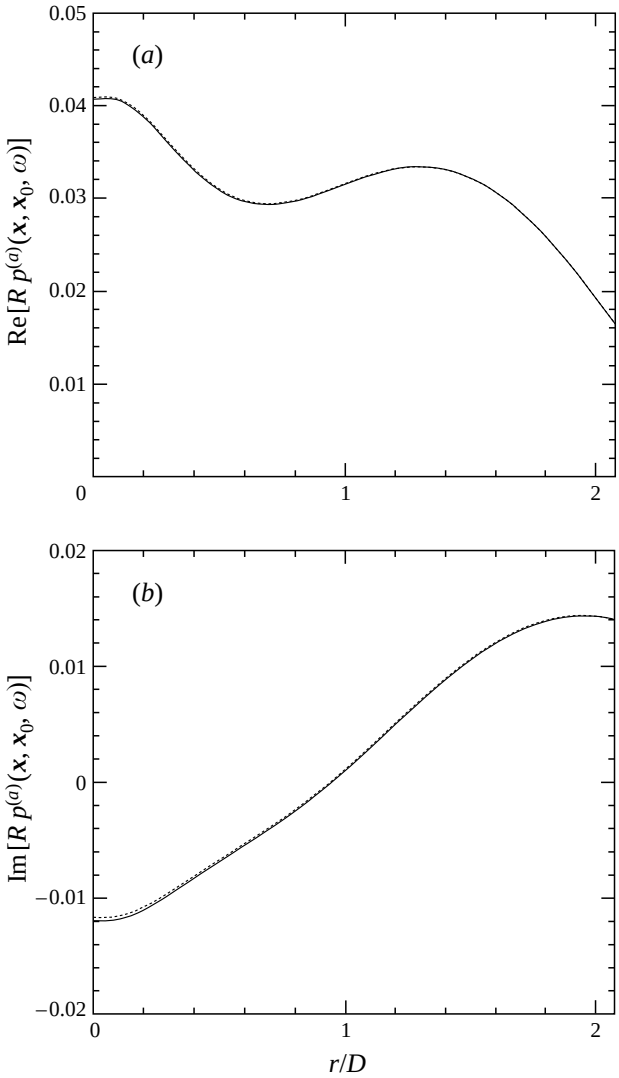

FIGURE 9. Numerical solution of (*a*) the real part and (*b*) the imaginary part of $p^{(a)}(\boldsymbol{x}, \boldsymbol{x}_0, \omega)$. $\boldsymbol{x} = (r,\ \phi = 90^\circ,\ x = 6D)$, $\boldsymbol{x}_0 = (R = 100D, \Theta = 60^\circ, \phi = 0)$ $M_j = 0.9$, $T_r/T_\infty = 2.0$, $St = 0.3$. ———, Finite difference solution; · · · · · · · · , separation of variables solution.

comparable to that of figure 9 are found. This provides confidence in the accuracy of our finite difference time marching scheme.

5. Numerical results

It is obvious that there is a large disparity in the level of effort needed to carry out a parallel flow Green's function calculation and the corresponding fully non-parallel flow calculation. The former requires relatively little computation time. For this reason, it would be important and useful to find out how accurate the results based on the locally parallel flow approximation are. To clarify this point, we carried out an extensive parametric study comparing the directivities calculated using both the

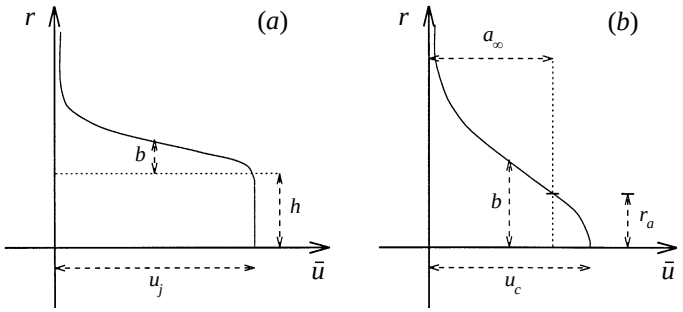

FIGURE 10. Mean velocity profiles of a jet: (*a*) core region, (*b*) developed region.

locally parallel flow approximation and the non-parallel flow finite difference method. In all these computations, the jet mean flows were determined by using the $k-\varepsilon$ turbulence model with modified coefficients as discussed by Thies and Tam (1996). As shown by Thies & Tam, the $k-\varepsilon$ turbulence model with modified coefficients can provide reliable mean jet flow velocity profiles over a wide range of jet Mach numbers and jet to ambient temperature ratios. It is known that the mean flow profile of a jet can be closely approximated by the following functions characterized by two parameters (see figure 10).

In the core region

$$\bar{u} = \begin{cases} u_j, & r < h \\ u_j \exp\left[-(\ln 2)\left(\dfrac{r-h(x)}{b(x)}\right)^2\right], & h \leqslant r, \end{cases} \tag{33}$$

where $h(x)$ is the radius of the uniform core and $b(x)$ is the half-width of the annulus mixing layer.

In the developed region

$$\bar{u} = u_c(x) \exp\left[-(\ln 2)\left(\frac{r}{b(x)}\right)^2\right], \tag{34}$$

where $u_c(x)$ is the centreline velocity and $b(x)$ is the half-width of the velocity profile. In an earlier work, Troutt & McLaughlin (1982) successfully used (33) and (34) to collapse their extensive jet mean velocity measurements. Tam & Burton (1984) and others, on the other hand, used these profiles for instability waves and jet noise calculations. Here we found that these profiles are in good agreement with those calculated numerically by the $k-\varepsilon$ turbulence model.

Two general results have emerged from the parametric study. First is that the cone of silence around the jet flow direction is strongly affected by the frequency of the acoustic waves under consideration. At low frequencies, the existence of a cone of silence for the radiated sound is not always apparent. On the other hand, at high frequencies, a well-defined cone of silence is, invariably, present. Second is that outside the cone of silence, the directivity given by the locally parallel flow approximation is sufficiently reliable that we recommend its usage whenever possible. But inside the cone of silence, caution must be exercised when such an approximation is employed. To illustrate this point, consider a Mach 0.9 jet at $T_r/T_\infty = 2.0$. The jet is supersonic relative to ambient sound speed near the nozzle exit. But sufficiently far downstream, with the decrease in velocity, the mean flow velocity is subsonic. Thus for such

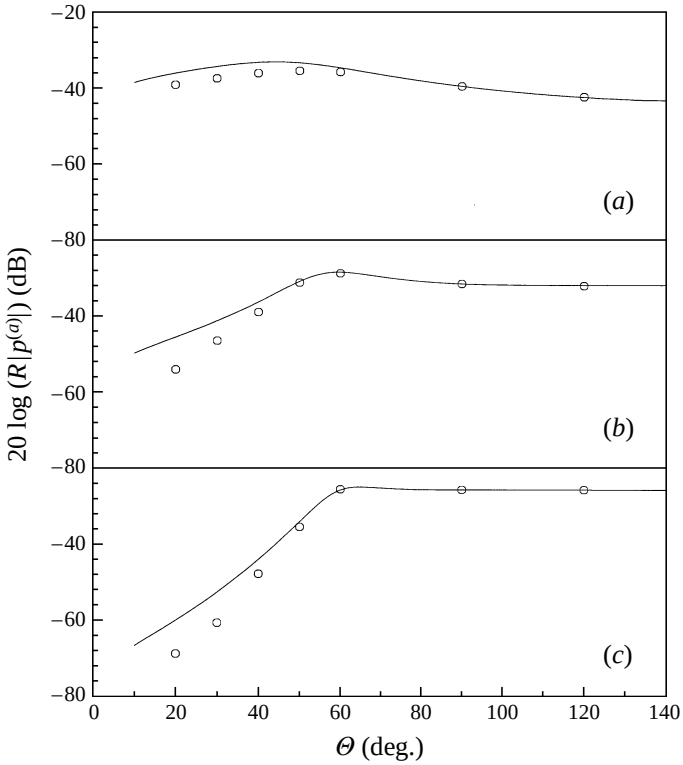

FIGURE 11. Comparisons between directivities of $p^{(a)}(\mathbf{x}_s, \boldsymbol{x}_0, \omega)$ calculated using parallel and non-parallel jet mean flow. $M_j = 0.9$, $T_r/T_\infty = 2.0$, $u_c/u_j = 0.84$, $h/D = 0$, $b/D = 0.65$. (*a*) $St = 0.1$, (*b*) $St = 0.3$, (*c*) $St = 0.6$. $\boldsymbol{x}_s = (r = 0, x = 8D,\ \phi = 0^\circ)$; $\boldsymbol{x}_0 = (R = 100D, \Theta, \phi = 0^\circ)$. ———, Parallel jet mean flow; o, non-parallel jet mean flow.

downstream locations, there is no critical direction of radiation (see the paragraph below) and the locally parallel flow solution can be calculated in a straightforward manner. Figure 11 shows the directivity of sound radiation by a point source located at the jet axis at 8 diameters downstream where the jet velocity is less than the ambient sound speed. At low Strouhal number, figure 11(*a*), the directivity is nearly flat. At medium to high Strouhal number, figures 11(*b*) and 11(*c*), a well-developed cone of silence is evident. In these figures, the full line is the result of the locally parallel flow solution. The circles are the non-parallel numerical solution. Outside the cone of silence, the two solutions are nearly identical. Inside the cone of silence, close to the jet axis, say at $\theta = 20^\circ$, the error in using the locally parallel flow assumption is quite large; as large as 9 dB at moderate to high Strouhal numbers. The reason why large error can occur when the locally parallel flow approximation is used for small radiation angle is easy to understand. Physically, at small radiation angle, the sound waves have to propagate over a long distance through the mean flow before leaving a parallel flow jet. Such, however, is not the case for a real divergent jet.

At locations closer to the nozzle exit, where a part of the jet mean flow is supersonic relative to ambient sound speed, a critical point exists in the locally parallel flow equations as discussed in § 2.2. The critical direction of radiation, θ_c, is given by

$$\theta_c = \cos^{-1}\left[\frac{a_\infty}{\overline{u}(r_c)}\right], \tag{35}$$

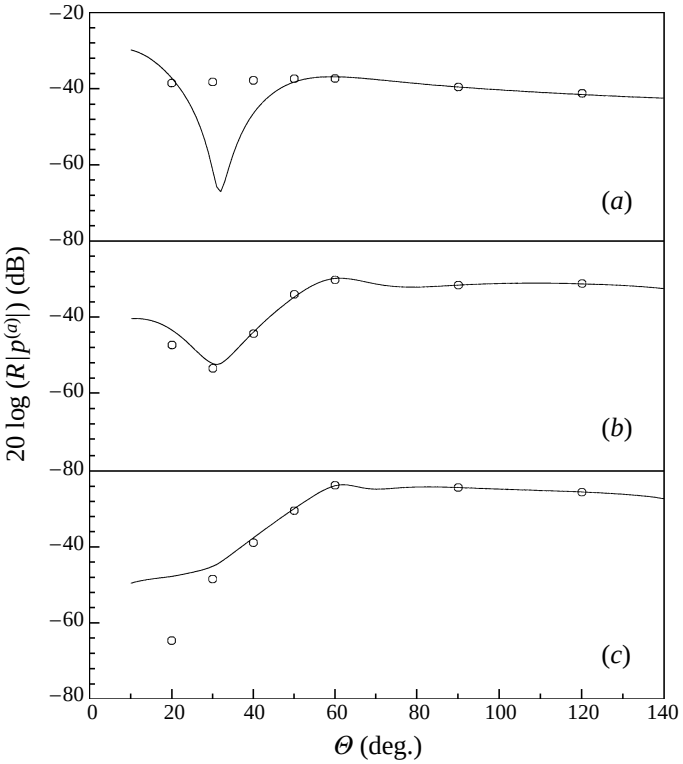

FIGURE 12. As figure 11 but $u_c/u_j = 1.0$, $h/D = 0.18$, $b/D = 0.38$.

where r_c is the radial location of the critical layer. The existence of the critical point tends to further downgrade the accuracy of the locally parallel flow approximation. To clarify this, let us consider the mean velocity profile of figure 10(*b*). The jet velocity from the centreline to a radial location $r = r_a$ is supersonic relative to the ambient sound speed. But for $r > r_a$, the jet velocity is subsonic. Now according to (35) r_c, the location of the critical layer, can be anywhere from $r = 0$ to r_a. Its precise location, of course, depends on the direction of radiation. Because of this, two cases arise depending on whether the source point is located inside or outside r_a. If the source point is located outside r_a then the critical point r_c cannot be located at the same point. In this case, the locally parallel flow approximation together with the contour deformation method (deformed around the critical point r_c) would yield a continuous directivity curve. As an example, let us return to the Mach 0.9 jet at temperature ratio 2.0. At four diameters downstream, the jet centreline velocity is faster than the ambient sound speed. However, at $r = 0.5D$ the mean flow velocity is subsonic with respect to ambient sound velocity. Figure 12 shows the calculated directivities for the noise source located at $r = 0.5D$ ($r > r_a$) using the locally parallel flow approximation (full line) and the non-parallel flow numerical approach (circles). It can be seen that there are substantial discrepancies inside the cone of silence both at low and high Strouhal numbers. It is to be noted that the nature of the errors here is not the same as that of figure 11. They are due primarily to the existence of a critical point in the governing equations.

Now if the noise source is located closer to the jet axis where r is less than r_a, the locally parallel flow approximation encounters further difficulty. There will be a

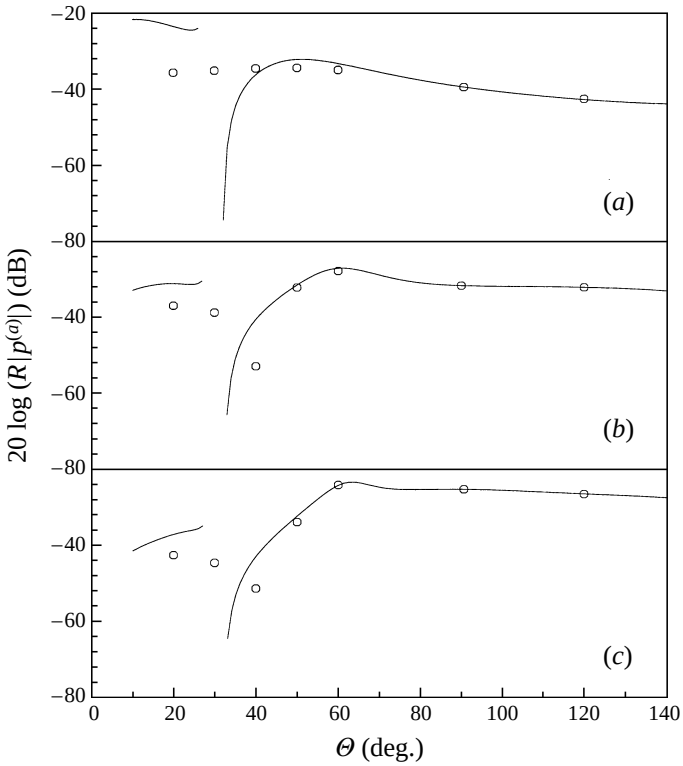

FIGURE 13. As figure 11 but $\boldsymbol{x}_s = (r = 0.25D,\ x = 4D, \phi = 0°)$.

direction of radiation for which the critical point r_c coincides with the source point. Under this circumstance, the solution cannot reach the source point by the contour deformation method (the contour is deformed around it). What this means is that the locally parallel flow approximation fails to provide a solution for the critical direction of radiation. As a result, there is a missing direction in the directivity curve. Figure 13 shows the directivity curve for a source located at $x = 4D$, $r = 0.25D$ ($r < r_a$) calculated by the locally parallel flow method and the non-parallel flow numerical method. The directivity of the parallel flow calculation behaves well outside the cone of silence but exhibits the features of a discontinuity around the missing critical direction. On comparing with the non-parallel flow results, the error is very large and unacceptable. We strongly recommend against the use of the locally parallel flow model for radiation directions for which r_c is close to the source point.

6. Summary and discussion

In this paper, a new way to determine the mean flow refraction effect on sound radiated by localized sources inside a jet using the adjoint Green's function and the reciprocity relation is proposed. Significant savings in computational effort can be realized by adopting this new approach. Most previous works on this subject are based on the locally parallel flow approximation. The fully non-parallel flow effects can, however, be included in the present methods by calculating the adjoint Green's function using computational aeroacoustics algorithms. In the adjoint problem, the source point is not inside the jet. Thus, it would not be necessary for the time

marching numerical computation to resolve the source singularity. This is important in ensuring an accurate numerical solution.

Numerical results obtained in the present investigation indicate that the locally parallel flow approximation, widely used in the literature, can provide accurate directivity results outside the cone of silence. Caution, however, must be invoked when applying this approximation to radiation directions inside the cone of silence and especially for angular directions close to the jet axis.

Although in this work we have confined our study primarily to axisymmetric jets, it is clear that the reciprocity principle can also be used for non-axisymmetric jets. For non-axisymmetric jets, a full three-dimensional numerical computation is necessary. This, inevitably, would be very involved and costly. But if the locally parallel flow approximation is deemed adequate, then only a much simpler two-dimensional time-domain computation would be required. Such calculations are feasible using present day computers.

This work was supported by the NASA Lewis Research Center Grant NAG 3-1683.

Appendix A. Reciprocity relations for the linearized Euler equations

Our primary concern here is the mean flow refraction effect on noise from fine-scale turbulence in jets. Since fine-scale turbulence does not introduce extra mass into the flow, we will only consider Green's function for time-periodic momentum sources (i.e. a term $(1/2\pi)\delta(\boldsymbol{x}-\boldsymbol{x}_0)\,\mathrm{e}^{-\mathrm{i}\omega t}$ is added to the momentum equations). Attention will be directed to the spatial part of the time-periodic Green's function. We will use superscript (n), $n = 1, 2, 3$ to denote the Green's function corresponding to a momentum source term added to the x, y, and z momentum equations respectively. Upon factoring out $\mathrm{e}^{-\mathrm{i}\omega t}$, the linearized Euler and energy equations in Cartesian tensor subscript notation are

$$-\mathrm{i}\omega\rho^{(n)} + \frac{\partial}{\partial x_j}\left(\overline{\rho}\, v_j^{(n)} + \rho^{(n)}\,\overline{v}_j\right) = 0, \tag{A 1}$$

$$-\mathrm{i}\omega\,\overline{\rho}\, v_i^{(n)} - \mathrm{i}\omega\rho^{(n)}\,\overline{v}_i + \frac{\partial}{\partial x_j}\left(\overline{\rho}\,\overline{v}_i\, v_j^{(n)} + \overline{\rho}\, v_i^{(n)}\,\overline{v}_j + \rho^{(n)}\,\overline{v}_i\,\overline{v}_j\right) + \frac{\partial p^{(n)}}{\partial x_i} = \frac{1}{2\pi}\delta_{ni}\delta(\boldsymbol{x}-\boldsymbol{x}_s), \tag{A 2}$$

$$-\mathrm{i}\omega p^{(n)} + \frac{\partial}{\partial x_j}\left(\overline{p}\, v_j^{(n)} + p^{(n)}\,\overline{v}_j\right) + (\gamma-1)\,\overline{p}\,\frac{\partial v_j^{(n)}}{\partial x_j} + (\gamma-1)\,p^{(n)}\frac{\partial\,\overline{v}_j}{\partial x_j} = 0, \tag{A 3}$$

where δ_{ni} is the Kronecker delta.

Without loss of generality, we will assume that there are solid bodies with surfaces S_1 and S_2 in the domain as shown in figure 14. On these surfaces, the boundary conditions are

$$\overline{v}_j\, n_j = 0, \quad v_j^{(n)} n_j = 0 \tag{A 4}$$

where n_j is the outward pointing unit normal of the surfaces.

To find the equations and boundary conditions for the adjoint Green's function, let us multiply (A 1), (A 2) and (A 3) by functions $\rho^{(a)}(\boldsymbol{x}, \boldsymbol{x}_0, \omega)$, $v^{(a)}(\boldsymbol{x}, \boldsymbol{x}_0, \omega)$ and $p^{(a)}(\boldsymbol{x}, \boldsymbol{x}_0, \omega)$ respectively and integrate over the volume V, see figure 12, external to all the solid surfaces. Upon adding the three equations together and after some simple

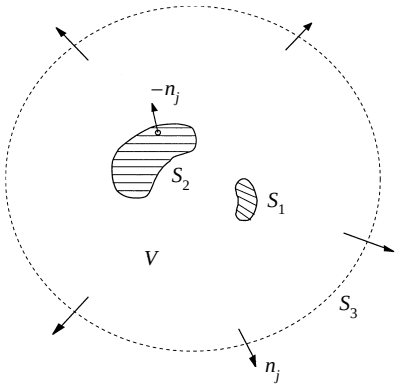

FIGURE 14. Schematic diagram showing the presence of solid bodies with bounding surfaces S_1 and S_2 in the physical domain.

algebraic manipulation, it is easy to derive the following equation:

$$\begin{aligned}
&\iiint_V \Bigg\{ \left[-\mathrm{i}\omega\rho^{(a)} - \overline{v}_j \frac{\partial \rho^{(a)}}{\partial x_j} + \overline{v}_j v_i^{(a)} \frac{\partial \overline{v}_i}{\partial x_j} \right] \rho^{(n)} \\
&\quad + \Bigg[-\overline{\rho} \frac{\partial \rho^{(a)}}{\partial x_i} - i\omega \overline{\rho} v_i^{(a)} + \overline{\rho} v_j^{(a)} \frac{\partial \overline{v}_j}{\partial x_i} \\
&\quad - \overline{\rho}\, \overline{v}_j \frac{\partial v_i^{(a)}}{\partial x_j} - \overline{p} \frac{\partial p^{(a)}}{\partial x_i} - (\gamma - 1) \frac{\partial}{\partial x_i} \left(\overline{p} p^{(a)} \right) \Bigg] v_i^{(n)} \\
&\quad + \left[-\mathrm{i}\omega p^{(a)} - \frac{\partial v_j^{(a)}}{\partial x_j} - \overline{v}_j \frac{\partial p^{(a)}}{\partial x_j} + (\gamma - 1) p^{(a)} \frac{\partial \overline{v}_j}{\partial x_j} \right] p^{(n)} \Bigg\} \mathrm{d}V \\
&\quad + \iiint_V \frac{\partial}{\partial x_j} \Bigg[\left(\overline{\rho} v_j^{(n)} + \rho^{(n)} \overline{v}_j \right) \rho^{(a)} - \left(\overline{\rho} v_j^{(n)} + \rho^{(n)} \overline{v}_j \right) \overline{v}_i v_i^{(a)} \\
&\quad + \left(\overline{\rho}\, \overline{v}_i v_j^{(n)} + \overline{\rho} v_i^{(n)} \overline{v}_j + \rho^{(n)} \overline{v}_i \overline{v}_j \right) v_i^{(a)} + p^{(n)} v_j^{(a)} + p^{(n)} \overline{v}_j p^{(a)} + \gamma v_j^{(n)} \overline{p}\, p^{(a)} \Bigg] \mathrm{d}V \\
&= \frac{\delta_{ni}}{2\pi} v_i^{(a)} (\boldsymbol{x}_s, \boldsymbol{x}_0, \omega). \qquad \text{(A 5)}
\end{aligned}$$

We will now choose the functions $\rho^{(a)}$, $v_i^{(a)}$ and $p^{(a)}$ to be the solution of the adjoint equations defined below:

$$-\mathrm{i}\omega\rho^{(a)} - \overline{v}_j \frac{\partial \rho^{(a)}}{\partial x_j} + \overline{v}_j v_i^{(a)} \frac{\partial \overline{v}_i}{\partial x_j} = 0, \qquad \text{(A 6)}$$

$$-\mathrm{i}\omega \overline{\rho} v_i^{(a)} - \overline{\rho} \frac{\partial \rho^{(a)}}{\partial x_i} + \overline{\rho} v_j^{(a)} \frac{\partial \overline{v}_j}{\partial x_i} - \overline{\rho}\, \overline{v}_j \frac{\partial v_i^{(a)}}{\partial x_j} - \overline{p} \frac{\partial p^{(a)}}{\partial x_i} - (\gamma - 1) \frac{\partial \overline{p} p^{(a)}}{\partial x_i} = 0, \qquad \text{(A 7)}$$

$$-\mathrm{i}\omega p^{(a)} - \frac{\partial v_j^{(a)}}{\partial x_j} - \overline{v}_j \frac{\partial p^{(a)}}{\partial x_j} + (\gamma - 1) p^{(a)} \frac{\partial \overline{v}_j}{\partial x_j} = \frac{1}{2\pi} \delta (\boldsymbol{x} - \boldsymbol{x}_0). \qquad \text{(A 8)}$$

By means of (A 6) to (A 8), the first integral of (A 5) can be evaluated. It is equal to $(1/2\pi) p^{(n)} (\boldsymbol{x}_0, \boldsymbol{x}_s, \omega)$. The second integral of (A 5), denoted as J_2, can be casted into

a surface integral by means of the divergence theorem. By choosing the boundary condition on the solid surface for the adjoint $v_i^{(a)}$ to be

$$v_i^{(a)} n_i = 0, \tag{A 9}$$

It is easy to find, together with boundary condition (A 4), that the integrand of the surface integral over the solid surfaces is zero. Hence only the outer surface integral over surface S_3 remains. That is,

$$J_2 = \iint_{S_3} \left[\left(\overline{\rho}\, v_j^{(n)} + \rho^{(n)}\, \overline{v}_j \right) \rho^{(a)} - \left(\overline{\rho}\, v_j^{(n)} + \rho^{(n)}\, \overline{v}_j \right) \overline{v}_i\, v_i^{(a)} \right.$$
$$\left. + \left(\overline{\rho}\, \overline{v}_i\, v_j^{(n)} + \overline{\rho}\, v_i^{(n)}\, \overline{v}_j + \rho^{(n)}\, \overline{v}_i\, \overline{v}_j \right) v_i^{(a)} + p^{(n)} v_j^{(a)} + p^{(n)}\, \overline{v}_j\, p^{(a)} + \gamma v_j^{(n)}\, \overline{p}\, p^{(a)} \right] n_j \, \mathrm{d}S. \tag{A 10}$$

Now let us push the surface S_3 to infinity. We note that the mean flow of the jet may be created by mass or momentum sources so that for large R, $\overline{v}_j = O\left(1/R^2\right)$. Also $v_j^{(n)}$ are the velocity components of the acoustic field, thus $v_j^{(n)} = O\left(1/R\right)$ as $R \to \infty$. By means of (A 6) to (A 8) it can be shown that the adjoint solution has the following asymptotic behaviour:

$$R \to \infty, \quad p^{(a)}, v_j^{(a)} = O\left(\frac{1}{R}\right), \quad \rho^{(a)} = O\left(\frac{1}{R^2}\right). \tag{A 11}$$

By means of the asymptotic behaviour of the original and the adjoint solutions, it is readily shown that the integrand of (A10) is of the order of $1/R^3$ as $R \to \infty$. Therefore, in the limit $S_3 \to \infty$, J_2 goes to zero. Equation (A5) thus leads to the following reciprocity relation:

$$p^{(n)}(\boldsymbol{x}_0, \boldsymbol{x}_s, \omega) = \delta_{ni} v_i^{(a)}(\boldsymbol{x}_s, \boldsymbol{x}_0, \omega). \tag{A 12}$$

That is, the pressure Green's functions ($n = 1, 2, 3$) of the linearized Euler equations can be found from the adjoint velocity field. (Note: the adjoint velocity does not have the same meaning as physical velocity.)

Appendix B. Non-homogeneous terms

The non-homogeneous terms of equation (31) are

$$I_1 = \left[-\left(\overline{v}\, \frac{\partial\, \overline{v}}{\partial r} + \overline{u}\, \frac{\partial\, \overline{v}}{\partial x} \right) \frac{\omega \sin \Theta}{a_\infty} J_m' \left(\frac{\omega \sin \Theta}{a_\infty} r \right) \right.$$
$$\left. + \left(\overline{v}\, \frac{\partial\, \overline{u}}{\partial r} + \overline{u}\, \frac{\partial\, \overline{u}}{\partial x} \right) \frac{\mathrm{i}\omega \cos \Theta}{a_\infty} J_m \left(\frac{\omega \sin \Theta}{a_\infty} r \right) \right] \exp\left(\mathrm{i}\omega \left(\frac{x \cos \Theta}{a_\infty} - t \right) \right),$$

$$I_2 = \left[\omega \cos \Theta \left(\overline{\rho} - \frac{\gamma\, \overline{p}}{a_\infty^2} \right) - \mathrm{i}\, \overline{u} \cos \Theta \left(\frac{\partial\, \overline{\rho}}{\partial x} - \overline{\rho}\, \frac{\mathrm{i}\omega \cos \Theta}{a_\infty} \right) \right.$$
$$\left. - \frac{\mathrm{i} \cos \Theta}{r} \frac{\partial\, (\overline{\rho}\, \overline{v}\, r)}{\partial r} - (\gamma - 1) \frac{\mathrm{i}}{a_\infty} \frac{\partial\, \overline{p}}{\partial x} \right] \frac{\omega}{a_\infty} J_m \left(\frac{\omega \sin \Theta}{a_\infty} r \right)$$
$$- \left(\overline{\rho}\, \frac{\partial\, \overline{v}}{\partial x} + \mathrm{i}\, \overline{\rho}\, \frac{\overline{v}\, \omega \cos \Theta}{a_\infty} \right) \frac{\omega \sin \Theta}{a_\infty} J_m' \left(\frac{\omega \sin \Theta}{a_\infty} r \right) \Bigg] \exp\left(\mathrm{i}\omega \left(\frac{x \cos \Theta}{a_\infty} - t \right) \right),$$

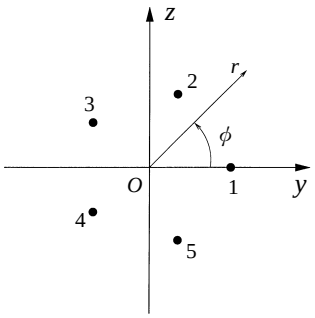

FIGURE 15. Location of noise sources at the $(x = 0)$-plane.

$$I_3 = \left\{ \left(\overline{\rho}\,\frac{\partial \overline{u}}{\partial r}\cos\Theta - \frac{(\gamma-1)}{a_\infty}\frac{\partial \overline{p}}{\partial r}\right)\frac{\mathrm{i}\omega}{a_\infty}J_m\left(\frac{\omega\sin\Theta}{a_\infty}r\right)\right.$$
$$+\left[\mathrm{i}\omega\left(\overline{\rho}-\frac{\gamma\,\overline{p}}{a_\infty}\right)+\frac{\partial\,\overline{\rho}}{\partial r}\,\overline{v}+\frac{\overline{\rho}\,\overline{v}}{r}+\frac{\partial\,\overline{\rho}\,\overline{u}}{\partial x}-\mathrm{i}\,\overline{\rho}\,\overline{u}\,\frac{\omega\cos\Theta}{a_\infty}\right]\times\frac{\omega\sin\Theta}{a_\infty}J'_m\left(\frac{\omega\sin\Theta}{a_\infty}r\right)$$
$$\left.+\,\overline{\rho}\,\overline{v}\,\frac{\omega^2\sin^2\Theta}{a_\infty^2}J''_m\left(\frac{\omega\sin\Theta}{a_\infty}r\right)\right\}\exp\left(\mathrm{i}\omega\left(\frac{x\cos\Theta}{a_\infty}-t\right)\right),$$

$$I_4 = \left\{\left[-\mathrm{i}\omega\,\overline{\rho}-\frac{\partial\,\overline{\rho}\,\overline{v}}{\partial r}-\frac{\partial\,\overline{\rho}\,\overline{u}}{\partial x}+\overline{\rho}\,\overline{u}\,\frac{\mathrm{i}\omega\cos\Theta}{a_\infty}+\frac{\gamma\,\overline{p}\,\mathrm{i}\omega}{a_\infty^2}\right]\frac{m}{r}J_m\left(\frac{\omega\sin\Theta}{a_\infty}r\right),\right.$$
$$\left.-\frac{m}{r}\,\overline{\rho}\,\overline{v}\,\frac{\omega\sin\Theta}{a_\infty}J'_m\left(\frac{\omega\sin\Theta}{a_\infty}r\right)\right\}\exp\left(\mathrm{i}\omega\left(\frac{x\cos\Theta}{a_\infty}-t\right)\right),$$

$$I_5 = \left\{\left[\frac{\omega^2}{a_\infty^2}\sin^2\Theta-\frac{m^2}{r^2}+\frac{\mathrm{i}\omega}{a_\infty^2}\left(\frac{1}{r}\frac{\partial\,(\overline{v}\,r)}{\partial r}+\frac{\partial\,\overline{u}}{\partial x}\right)(\gamma-1)\right.\right.$$
$$\left.-\frac{\overline{u}\,\omega^2\cos\Theta}{a_\infty^3}\right]J_m\left(\frac{\omega\sin\Theta}{a_\infty}r\right)+\left(\frac{1}{r}-\frac{\mathrm{i}\omega\,\overline{v}}{a_\infty^2}\right)\frac{\omega\sin\Theta}{a_\infty}J'_m\left(\frac{\omega\sin\Theta}{a_\infty}r\right)$$
$$\left.+\frac{\omega^2\sin^2\Theta}{a_\infty^2}J''_m\left(\frac{\omega\sin\Theta}{a_\infty}r\right)\right\}\exp\left(\mathrm{i}\omega\left(\frac{x\cos\Theta}{a_\infty}-t\right)\right). \qquad \text{(B 1)}$$

Appendix C. Multiple sources – an example

A concrete example involving multiple sources is provided in this Appendix to illustrate the great savings in computation that can be realized by using the reciprocity relation and the adjoint Green's function. We will consider a parallel flow jet with a velocity profile given by (34) as shown figure 10(*b*). The centreline Mach number (M_j) is taken to be 0.9 and the jet to ambient temperature ratio is 1.0. The half-width of the jet velocity profile will be labelled as b, the characteristic length of the problem. Five axial momentum sources (see equation (20)), all located on the $(x = 0)$-plane, are distributed in the (y, z)-plane as shown in figure 15. Let $(r_j, \phi_j, 0)$, $j = 1, 2, \ldots, 5$, be the cylindrical coordinates of the source and A_j be the corresponding weighting

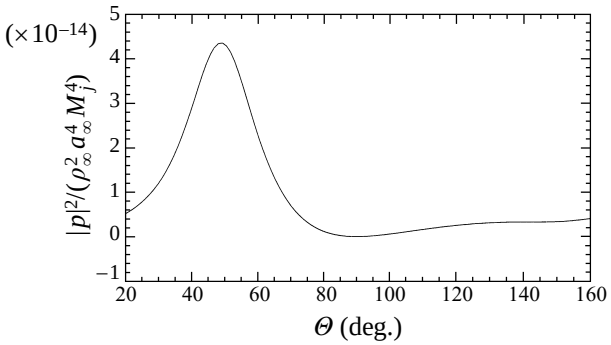

FIGURE 16. Far-field pressure distribution generated by five axial momentum sources inside a parallel jet. $M_j = u_c/a_j = 0.9$, $T_r/T_\infty = 1.0$, $fb/u_c = 0.3$, $\boldsymbol{x} = (R = 100b, \Theta, \phi = 0°)$. ————, Calculation using the direct Green's function; · · · · · · · · , calculation using the adjoint Green's function (indistinguishable).

factor. The numerical values chosen for the example are

$$r_j = b, \quad \phi_j = (j-1)\frac{2\pi}{5}, \quad A_j = \rho_\infty a_\infty^2 M_j^2 b^2 j \times 10^{-6}, \quad j = 1, 2, \ldots, 5.$$

The radiated sound field at Strouhal number $fb/u_c = 0.3$ on the ($\phi = 0$)-plane is calculated in two ways. First, the direct Green's function of equation (20) is solved by separation of variables for each source. That is, the calculation is repeated five times. They are summed to provide the combined field. Second, the adjoint equation (25) is solved. The radiated pressure field is determined by (24). In this approach, one calculation is needed. Figure 16 shows the calculated directivities of the radiated sound pressure intensity. Both approaches give the same directivity up to 3 significant figures. However, the direct Green's function method takes about five times more computation.

REFERENCES

ATVARS, J., SCHUBERT, L. K. & RIBNER, H. S. 1965 Refraction of sound from a point source placed in an air jet. *J. Acoust. Soc. Am.* **37**, 168–170.

BALSA, T. F. 1976 The far field of high frequency convected singularities in sheared flows with an application to jet noise prediction. *J. Fluid Mech.* **74**, 193–208.

BALSA, T. F. 1977 The acoustic field of sources in shear flow with application to jet noise: convective amplification. *J. Fluid Mech.* **79**, 33–47.

CHANDRASEKHAR, S. 1989 Adjoint differential systems in the theory of hydrodynamic stability. In *Selected Papers of S. Chandrasekhar*, vol. 4, pp. 221–228. University of Chicago Press.

CHO, Y. C. 1980 Reciprocity principle in duct acoustics. *J. Acoust. Soc. Am.* **67**, 1421–1426.

DOWLING, A. P. 1983 Flow-acoustic interaction near a flexible wall. *J. Fluid Mech.* **128**, 181–198.

DURBIN, P. A. 1983*a* High frequency Green's function for aerodynamic noise in moving media, Part I: general theory. *J. Sound Vib.* **91**, 519–525.

DURBIN, P. A. 1983*b* High frequency Green's function for aerodynamic noise in moving media, Part II: noise from a spread jet. *J. Sound Vib.* **91**, 527–538.

ECKHAUS, W. 1965 *Studies in Nonlinear Stability Theory*. Springer.

GOLDSTEIN, M. E. 1975 The low frequency sound from multiple sources in axisymmetric shear flows. *J. Fluid Mech.* **70**, 595–604.

GOLDSTEIN, M. E. 1976 The low frequency sound from multiple sources in axisymmetric shear flows. Part 2. *J. Fluid Mech.* **75**, 17–28.

Goldstein, M. E. 1982 High frequency sound emission from moving point multiple sources embedded in arbitrary tranversely sheared mean flows. *J. Sound Vib.* **80**, 499–522.

Grande, E. 1965 Refraction of injected sound by a very cold nitrogen jet. *J. Acoust. Soc. Am.* **38**, 1063–1064.

Hill, D. C. 1995 Adjoint systems and their role in the receptivity problem for boundary layers. *J. Fluid Mech.* **292**, 183–204.

Howe, M. S. 1975 The generation of sound by aerodynamic sources in an inhomogeneous steady flow. *J. Fluid Mech.* **67**, 597–610.

Howe, M. S. 1978 A review of trailing edge noise. *J. Sound Vib.* **61**, 437–465.

Howe, M. S. 1981 The displacement-thickness theory of trailing edge noise. *J. Sound Vib.* **75**, 239–250.

Hixon, R., Shih, S. H. & Mankbadi, R. R. 1995 Evaluation of boundary conditions for computational aeroacoustics. *AIAA J.* **33** 2006–2012.

Khavaran, A. 1996 Refraction and shielding of noise in non-axisymmetric jets. *AIAA Paper* 96–1780.

Khavaran, A. & Krejsa, E. A. 1993 Propagation of high frequency jet noise using geometric acoustics. *AIAA Paper* 93–0147.

Khavaran, A. & Krejsa, E. A. 1994 Refraction of high frequency noise in an arbitrary jet flow. *AIAA Paper* 94–0139.

Magnus, W. & Oberhettinger, F. 1949 *Formulas and Theorems for the Functions of Mathematical Physics.* Chelsea Publishing Co. New York, NY.

Mani, R. 1976*a* The influence of jet flow on jet noise. Part 1. The noise of unheated jets. *J. Fluid Mech.* **76**, 753–778.

Mani, R. 1976*b* The influence of jet flow on jet noise. Part 2. The noise of heated jets. *J. Fluid Mech.* **76**, 779–793.

Roberts, P. H. 1960 Characteristic value problems posed by differential equations arising in hydrodynamics and hydromagnetics. *J. Math. Anal. Applics.* **1**, 193–214.

Schubert, L. K. 1972 Numerical study of sound refraction by a jet flow. I. Ray Acoustics. *J. Acoust. Soc. Am.* **51**, 439–446.

Tam, C. K. W. 1975 Supersonic jet noise generated by large scale disturbances. *J. Sound Vib.* **38**, 51–79.

Tam, C. K. W. 1995 Computational aeroacoustics: Issued and methods. *AIAA J.* **33**, 1778–1796.

Tam, C. K. W. & Burton, D. E. 1984 Sound generated by instability waves of supersonic flows. Part 2. Axisymmetric jets. *J. Fluid Mech.* **138**, 273–295.

Tam, C. K. W. & Morris, P. J. 1980 The radiation of sound by instability waves of a compressible plane turbulent shear layer. *J. Fluid Mech.* **98**, 349–381.

Tam, C. K. W. & Webb, J. C. 1993 Dispersion-relation-preserving finite difference scheme for computational acoustics. *J. Comput. Phys.* **107**, 262–281.

Tam, C. K. W., Webb, J. C. & Dong. Z. 1993 A study of the short wave components in computational acoustics. *J. Comput. Acoust.* **1**, 1–30.

Tester, B. J. & Morfey, C. L. 1976 Developments in jet noise modelling-theoretical predictions and comparisons with measured data. *J. Sound Vib.* **46**, 79–103.

Thies, A. T. & Tam, C. K. W. 1996 Computation of turbulent axisymmetric and nonaxisymmetric jet flows using the $k-\varepsilon$ model. *AIAA J.* **34**, 309–316.

Troutt, T. R. & McLaughlin, D. K. 1982 Experiments on the flow and acoustic properties of a moderate Reynolds number supersonic jet. *J. Fluid Mech.* **116**, 123–156.